Remote Sensing of Environment 263 (2021) 112542

Contents lists available at ScienceDirect

Remote Sensing of Environment

journal homepage: www.elsevier.com/locate/rse

Temperature effects on L-band vegetation optical depth of a boreal forest

Mike Schwank [a,b,*], Anna Kontu [c], Arnaud Mialon [e], Reza Naderpour [a], Derek Houtz [a,f], Juha Lemmetyinen [d], Kimmo Rautiainen [d], Qinghuan Li [g], Philippe Richaume [e], Yann Kerr [e], Christian Mätzler [b]

[a] Federal Research Institute for Forrest, Snow and Landscape Research WSL, Zürcherstrasse 111, Birmensdorf 8903, Switzerland
[b] GAMMA Remote Sensing Research and Consulting AG, Worbstr. 225, 3073 Gümligen, Switzerland
[c] Finnish Meteorological Institute, Arctic Space Centre, Tähteläntie 62, 99600 Sodankylä, Finland
[d] Finnish Meteorological Institute, Earth Observation Research, P.O.Box 503, 00101 Helsinki, Finland
[e] Center for the Study of the Biosphere from Space, 18 Avenue Édouard Belin 31401, Toulouse Cedex 9, France
[f] TerraRad Tech AG, Freilagerstrasse 97, 8047 Zürich, Switzerland
[g] Key Laboratory of Digital Earth Science, Aerospace Information Research Institute, Chinese Academy of Sciences, Beijing, China

ARTICLE INFO

Edited by: Jing M. Chen

Keywords:
Close-range L-band radiometry
Microwave remote sensing
Vegetation Optical Depth (VOD)
Two-stream Emission Model (2S EM)
Ground permittivity
SMOS
SMAP
Boreal forest

ABSTRACT

ElectroMagnetic (EM) reasons resulting in temperature dependence of L-band Vegetation Optical Depth (L-VOD) are currently overlooked in remote sensing products. Discrepancies in retrievals of geophysical surface properties over vegetated areas can result from this incompleteness. This perception motivated to explore EM considerations in how temperature drives L-VOD of a boreal forest. Thereto, a novel physics-based model is developed and evaluated to assess L-VOD sensitivities to canopy temperature and some other model parameters. The L-VOD model is compared to L-VOD derived from close-range L-band brightness temperatures measured through the tree canopy at the Finnish Meteorological Institute's Arctic Research Center (FMI-ARC) in Sodankylä (Finland) during a 4-week and a 1-day period in 2019. Furthermore, the model's ability to explain L-VOD retrieved from brightness temperatures of the "Soil Moisture and Ocean Salinity" (SMOS) satellite over the "Sodankylä grid cell" is investigated. Experimental L-VOD are maximal at around 0 °C and decrease when canopy temperature is moving away from zero degree Celsius. This temperature response, observed at different temporal- and spatial scales, is captured by the proposed L-VOD model and explained by freezing tree sap-water and the dependence of water permittivity on temperature. The demonstrated EM-induced temperature dependence suggest caution with interpreting satellite-based L-VOD, because increased L-VOD around the freezing point is not solely due to increased biomass or rehydration of the vegetation. Further, our study can find future application to compensate L-VOD for EM-induced temperature sensitivity. This potentially leads to improved explanatory power of temperature normalized L-VOD for characterization of forest phenology. Furthermore, we suggest examining the presence and strength of the demonstrated L-VOD temperature response as a practical L-VOD retrieval quality assessment method under steady forest phenology.

1. Introduction

Temperate-, tropical- and boreal forests cover more than 30 % of the Earth's land surface. Their areal extent and phenology affects the exchange of radiative energy, water (via evapotranspiration and infiltration/runoff), and trace gases (water vapor and CO_2) between the ground and the atmosphere (Richardson et al., 2013). Respective exchange rates play a major role in global and regional climate systems, which in turn feedback on forest phenology and extent. Timing of spring thaw determines the length of the growing season of boreal forests at high latitudes, whose greening period has extended throughout the last decades due to global warming (Jia et al., 2009). There are indications that earlier spring snow-melt has increased the overall carbon uptake of boreal forests (Pulliainen et al., 2017). It is still disputed if the resulting

* Corresponding author at: Federal Research Institute for Forrest, Snow and Landscape Research WSL, Zürcherstrasse 111, Birmensdorf 8903, Switzerland.
E-mail addresses: mike.schwank@wsl.ch (M. Schwank), anna.kontu@fmi.fi (A. Kontu), arnaud.mialon@cesbio.cnes.fr (A. Mialon), reza.naderpour@wsl.ch (R. Naderpour), derek.houtz@wsl.ch (D. Houtz), juha.lemmetyinen@fmi.fi (J. Lemmetyinen), Kimmo.Rautiainen@fmi.fi (K. Rautiainen), q97li@uwaterloo.ca (Q. Li), philippe.richaume@cesbio.cnes.fr (P. Richaume), yann.kerr@cesbio.cnes.fr (Y. Kerr), matzler@gamma-rs.ch (C. Mätzler).

https://doi.org/10.1016/j.rse.2021.112542
Received 27 January 2021; Received in revised form 17 May 2021; Accepted 28 May 2021
Available online 24 June 2021

net carbon flux of this second largest biome is enhanced or dampened through various feedbacks (Magnani et al., 2007). However, there is a consensus that the altered duration of boreal forests' greening period, at the large scale, impact ground-atmosphere fluxes to a degree that is relevant for the future climate (Chapin Iii et al., 2000). Accordingly, remotely sensed forest phenology becomes increasingly important to further constrict modeled climate scenarios.

The most commonly used vegetation remote sensing products are the Normalized Difference Vegetation Index (NDVI) derived from reflectance at Near InfraRed (NIR) and red (Tucker, 1979), and the Enhanced Vegetation Index (EVI) computed from NIR, red, and blue reflectance (Huete et al., 1994). NDVI and EVI are proxies for photosynthetic activity (Kawabata et al., 2001; Zhang et al., 2003; Zhou et al., 2001), tree productivity (Wang et al., 2004), Leaf Area Index (LAI) (Wang et al., 2005), and areal vegetation cover (Carlson and Ripley, 1997). Compared to NDVI and EVI, the so-called Vegetation Optical Depth (VOD) contains complementary information on vegetation phenology, most importantly Vegetation Water Content (VWC) and Above-Ground Biomass (AGB). Table 1 in the recent review article (Frappart et al., 2020) provides a list of satellite Earth observation missions which were used, or could be used, to retrieve VOD at different microwave frequencies f ranging from the L-band ($f = 1 - 2$ GHz) to the Ka-band ($f = 27 - 40$ GHz). The European Space Agency (ESA) also plans to launch the 7th Earth Explorer mission BIOMASS in 2021 with the primary objective of global measurements of forest AGB (Scipal et al., 2010). The BIOMASS mission carries a Polarimetric Interferometric P-band Synthetic Aperture Radar (Pol-InSAR) operating at 435 GHz. Because of increasing penetration depth with increasing observation wavelength $\lambda = c/f$ ($c = 3 \cdot 10^8$ m s^{-1}), L-band Vegetation Optical Depth (L-VOD) is applicable for quantification of state parameters of dense vegetation, such as forests, shrubs, maize or mulch to mention a few. L-VOD proved to be a valuable proxy for AGB (Rodríguez-Fernández et al., 2018) over Africa, for instance. However, this relationship is not as strong for forests at high latitudes as in temperate regions (Mialon et al., 2020). This needs further exploration, because it is still unclear whether it is due to phenological or ElectroMagnetic (EM) reasons resulting from strong Summer-Winter variability of environmental temperatures in high latitudes forests. These forests vary more temporally than tropical forests as they undergo much larger temperature variations, including freezing conditions. Beside the demonstrated value of L-VOD to assess phenology of dense vegetation, it is also crucial to retrieve state parameters of the underlying ground. This is because brightness temperature of a land surface is significantly impacted by L-VOD (Jackson and Schmugge, 1991). Accordingly, better understanding of EM-induced temperature dependence of L-VOD could also improve retrieval of soil moisture (Vittucci et al., 2018) or Snow Water Equivalent (SWE) (Foster et al., 2005).

It has been long known that permittivity of fresh wood depends on temperature (Torgovnikov, 1993). A recent study, performed in a boreal forest, showed that the dielectric constant of trees depends on temperature (Roy et al., 2020). The related reduce of L-VOD resulting from freezing was demonstrated by means of close-range brightness temperatures measured with an upward looking L-band radiometer operated at the forest ground and a tower-based L-band radiometer measuring from above the canopy. Moreover, a study using close-range radiometry through a tree specimen against the cold sky, showed that microwave transmissivity t_C of a forest Canopy at X-, Ku- and Ka-band is linked to prevailing Canopy temperature T_C (Li et al., 2019). With decreasing $T_C < 0$ °C, a quasi-linear increase of t_C was observed, while for $T_C > 0$ °C no significant temperature dependence $t_C(T_C)$ was found.

The goal of the presented study is to demonstrate temperature dependence $\tau_C(T_C)$ of L-VOD caused by EM reasons by the example of a boreal forest. To explore EM reasons segregated from tree phenological reasons, the study periods are selected during early spring 2019 to preclude changing L-VOD resulting from vegetation growth, for instance. More concretely, this study extends the aforementioned findings about L-VOD's temperature dependence in two respects by: i) developing of a novel physics-based L-VOD model to explain EM reasons of $\tau_C(T_C)$ under frozen and thawed conditions, and ii) exploring EM-induced temperature dependence of L-VOD retrieved from spaceborne passive L-band observations, as provided by ESA's "Soil Moisture and Ocean Salinity" (SMOS) mission (Kerr et al., 2001; Kerr et al., 2010).

In Section 2 we explain experimental aspects. Sections 3.1 outlines the method used to derive L-VOD from close-range brightness temperatures measured in the forest at the Finnish Meteorological Institute's Arctic Research Center (FMI-ARC) in Sodankylä (Finland). Section 3.2 explains the method used to retrieve simultaneously L-VOD and effective Ground permittivity (τ_C, ε_G) from SMOS brightness temperatures over the grid cell including FMI-ARC. Section 3.3 presents the developed L-VOD model and discusses its sensitivities with respect to T_C and some other model parameters. Experimental temperature dependence of L-VOD at the local-scale and at the SMOS scale is presented and discussed in Sections 4.1 and 4.2 together with optimally matching simulated L-VOD. Section 5 summarizes the study, draws the principal conclusions, and proposes future work and applications.

2. Data sets

2.1. Test site and study area

One part of this study explores ElectroMagnetic (EM) reasons for the dependence $\tau_C(T_C)$ of L-VOD on Canopy temperature T_C at the local-scale. Thereto, L-VOD is computed from Below-Canopy (B-C) L-band brightness temperatures $T^p_{B,B\text{-}C}$ at horizontal ($p = H$) and vertical ($p = V$) polarizations measured from ground level through the tree canopy against the cold sky, similarly to Guglielmetti et al., 2007; Li et al., 2019; Mätzler, 1994; Roy et al., 2020.

Fig. 1(a, b) show Finland and a zoom into the area of the FMI-ARC in Sodankylä (Finland). Fig. 1(c–e) show the forest test-site at FMI-ARC where close-range $T^p_{B,B\text{-}C}$ are measured by the Below-Canopy (B-C) ETH L-Band RAdiometer (ELBARA-II) (Schwank et al., 2010). The overview photo in Fig. 1(c) depicts the B-C L-band radiometer with its antenna Field-of-View (FoV) of $\sim \pm 8.8°$ at -6 dB sensitivity relative to boresight at the Zenith observation angle $\theta_{Zen} = 50°$ corresponding to the nadir angle $\theta = 180° - \theta_{Zen} = 130°$. During the experiment, another ELBARA-II radiometer was operated from the 21-m platform of the Integrated Carbon Observation System (ICOS) tower to measure upwelling Above-Canopy (A-C) L-band brightness temperatures $T^p_{B,A\text{-}C}$. The two ELBARA-II radiometers are operated in "swath scanning" configurations to measure close-range $T^p_{B,B\text{-}C}$ and $T^p_{B,A\text{-}C}$ at $30° \leq \theta \leq 180°$ from Below, and from Above, the tree Canopy of height $h_C \simeq 10$ m.

The primary plan behind this setup including the B-C and the A-C radiometers was to achieve ($\tau_C, \omega_C, \varepsilon_G$) of L-VOD, single scattering-albedo, and effective Ground permittivity from quasi-simultaneous $T_{B,B\text{-}C}{}^p$ and $T^p_{B,A\text{-}C}$. However, this plan was abandoned because multi-angle retrievals ($\tau_C, \omega_C, \varepsilon_G$) proved unreliable mainly due to the large variability of biomass within the FoV of the two radiometer antennas. Further, inspection of measurements performed by the A-C radiometer revealed that respective $T^p_{B,A\text{-}C}$ were often corrupted by Radio Frequency Interferences (RFI) caused by active microwave sensors operated from the tower at the same time, and due to technical problems with the A-C radiometer.

For these reasons, only downwelling $T^p_{B,B\text{-}C}$ measured by the B-C radiometer, at $\theta_{Zen} = 50°$, are used to achieve L-VOD τ_C of the FMI-ARC forest canopy. Nonetheless, the Picket-horn antenna (Pickett et al., 1984) of the A-C ELBARA-II is used to calibrate the B-C ELBARA-II. Thereto, the RadioMeter Assembly (RMA) of the B-C ELBARA-II is connected to the antenna of the A-C ELBARA-II radiometer to calibrate its internal Active Could Source (ACS) by means of sky measurements (Section 2.3.1).

Fig. 1(d) shows a plan view of the B-C ELBARA-II radiometer measuring downwelling $T^p_{B,B\text{-}C}$ at $\theta_{Zen} = 50°$. Locations of trees within the -6 dB FoV are indicated in green. Fig. 1(e) shows a photo of the tree

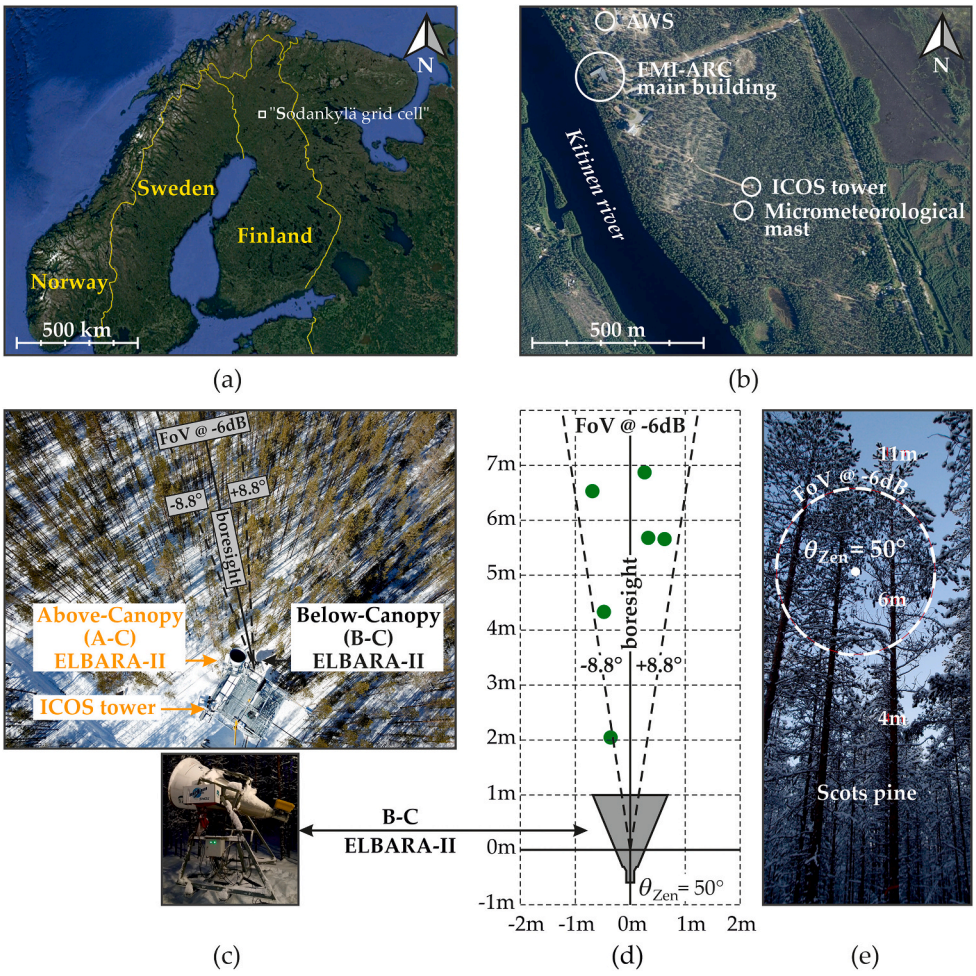

Fig. 1. (a, b) Location of the SMOS "Sodankylä grid cell" and a zoom into the area of the FMI-ARC in Sodankylä (Finland). (c) Overview photo of the forest-site at FMI-ARC including the two ELBARA-II L-band radiometers. The ~ ± 8.8° Field-of-View (FoV) at −6 dB sensitivity relative to boresight at the Zenith observation angle $\theta_{Zen} = 50°$ is indicated with dashed lines. (d) Plan view of the Below-Canopy (B-C) radiometer measuring downwelling brightness temperature $T^p_{B,B\text{-}C}$. Locations of trees within the FoV at $\theta_{Zen} = 50°$ are indicated in green. (e) Photo of the tree canopy taken from the location of the B-C radiometer, including the projected FoV at $\theta_{Zen} = 50°$.

canopy taken from the location of the B-C ELBARA-II including its projected antenna FoV for $\theta_{Zen} = 50°$.

The sparse population of Scots pine (*Pinus sylvestris*) is the prevailing tree species, as is typical of the dominant boreal forest in the larger surrounding of the FMI-ARC. Typical tree age in the area is between 60 and 160 years, with a mean AGB of 31 t ha^{-1} at a radius of ~ 20 km from FMI-ARC (information from Natural Resources Finland, www.luke.fi). According to the land cover classification applied for SMOS, the "Sodankylä grid cell" (67.3076°N, 26.5850°E, 625 km^2) provided at ~ 25 km × 25 km resolution (Al Bitar et al., 2017) and matching FMI-ARC (67.36236°N, 26.63862°E), exhibits the areal forest-fraction *FFO* = 93.5485 %. Remaining minor shares of land-classes are open-water *FWO* = 3.0167 % and low/sparse vegetation and wetlands *FNO* = 3.4348 % (Fernandez-Moran et al., 2017) (no Winter conditions considered). Representativeness of the tree species of the forest at FMI-ARC for the dominant land-class of the "Sodankylä grid cell" is important for the comparison between L-VOD's temperature dependence at the local-scale (Section 4.1) and the scale of SMOS (Section 4.2). Based on tree samples, the age of the trees in the forest stand observed by the B-C radiometer is between 80 and 160 years. Following a survey conducted in 2019, above-ground dry Column-Mass of the forest stand is $CM_{C,Dry} \cong 10$ kg m^{-2}. The soil at the forest stand site consists of mostly sandy podzols with a ~ 5 cm organic layer on top, covered with low (mostly < 5 cm) vegetation, mainly lichen (Cladonia stellaris), moss, lingonberry, and some sparse heather and crowberry. Fences keep large animals like reindeer from entering the forest and eating the lichen. The undergrowth mix, elsewhere within the wider Sodankylä area, consists mostly of the same species but with varying portions and typically less lichen. Accordingly, forest ground at the FMI-ARC might not well represent the natural forest ground within the SMOS "Sodankylä grid cell". However, this is not critical because local-scale L-VOD τ_C derived from $T^p_{B,B\text{-}C}$ are almost unaffected by forest ground properties (Section 3.1).

2.2. *In-situ measurements*

Time-series of in-situ Air temperature T_{Air} at two meters above ground, Tree skin-temperature T_{Tree}, and Soil temperatures $T_{Soil,5cm}$ and $T_{Soil,30cm}$ at 5 cm and 30 cm below the soil surface are used as follows: i) In Section 4.1 T_{Tree} and T_{Air} are used to compute L-VOD τ_C from close-range $T^p_{B,B\text{-}C}$ measured below the tree canopy at $\theta_{Zen} = 50°$. T_{Air} is used indirectly to simulate downwelling Sky radiance T_{Sky}. ii) In Section 4.2 $T_{Soil,5cm}$, $T_{Soil,30cm}$, and T_{Air} are used to retrieve L-VOD and effective Ground permittivity (τ_C, ε_G) from SMOS Level-3 Brightness Temperatures (L3TB) over the "Sodankylä grid cell" (Fig. 1(a)). Soil temperatures are used to compute effective Ground temperature T_G. Air temperature is used to simulate T_{Sky}, and to represent Canopy temperature $T_C = T_{Air}$.

Temperatures T_{Air}, $T_{Soil,5cm}$, and $T_{Soil,30cm}$ are measured with Pentronic PT100 sensors deployed at the "micrometeorological mast field" (Fig. 1(b)) at FMI-ARC ~ 70 m away from the ICOS tower where the close-range passive L-band observations are performed (Fig. 1(c–e)). From https://litdb.fmi.fi/met0010_data.php these data are available as 30-min averages dating back to 2005. Tree skin-temperatures are measured close by with 9 Decagon GS3 sensors drilled to 6 nearby trees. Five of the sensors are installed at 2 m above ground in neighboring trees, four sensors are installed at height 1 m, 2 m (at opposite sites) and

3 m of another tree. T_{Tree} used to represent Canopy temperature $T_{\mathrm{C}} = T_{\mathrm{Tree}}$ in the local-scale analysis are computed as averages of the 9 sensors' simultaneous readings available every 10 min. Further, Snow Depth (*SD*) is used in Section 4.2 in support of identifying the time-period appropriate for the analysis of SMOS-based L-VOD. *SD* is measured with Campbell Scientific SR50 sensors deployed at the FMI-ARC's operative Automatic Weather Station (AWS). Data from this AWS indicated in Fig. 1(b) are available from https://litdb.fmi.fi/luo0015_data.php.

2.3. Passive L-band data

2.3.1. Close-range ELBARA-II brightness temperatures

The first ELBARA (Mätzler et al., 2003), constructed by the Institute of Applied Physics (IAP) at University of Bern (Switzerland), was employed in a number of research projects to explore: L-band emission of freezing soil (Schwank et al., 2004), soils covered with low vegetation (Schwank et al., 2005), leaf litter (Schwank et al., 2008), and forest (Guglielmetti et al., 2007, 2008), effects of soil surface roughness (Schneeberger et al., 2004; Schwank and Mätzler, 2006) and macro-structure (Völksch et al., 2010, 2011; Völksch et al., 2015). The next generation ELBARA-II radiometers (Schwank et al., 2010) were developed for calibration/validation purposes of the SMOS mission (Kerr et al., 2001; Kerr et al., 2010). ELBARA-II and its successor ELBARA-III were deployed at numerous calibration/validation- and research sites in Spain (Fernandez-Moran et al., 2014; Miernecki et al., 2014; Schwank et al., 2012), France (Pellarin et al., 2016), Germany (Jonard et al., 2011), the Tibetan plateau (Su et al., 2020; Zheng et al., 2019a; Zheng et al., 2019b; Zheng et al., 2017), Switzerland (Naderpour and Schwank, 2018; Naderpour et al., 2017a; Naderpour et al., 2017b; Schwank and Naderpour, 2018), the Swiss-camp in Greenland (Naderpour et al., 2020), as well as at the FMI-ARC (Lemmetyinen et al., 2016a; Lemmetyinen et al., 2016b; Rautiainen et al., 2014).

Section 4.1 investigates the temperature dependence $\tau_{\mathrm{C}}(T_{\mathrm{C}})$ of L-VOD at the local-scale computed from close-range $T^{p}_{\mathrm{B,B\text{-}C}}$ measured with the B-C ELBARA-II (Fig. 1). The design and performance of the radiometer, as well as the methodology to achieve calibrated antenna temperatures is presented in Schwank et al., 2010. ELBARA-II is an analog power-detection microwave radiometer. The sensitive frequency range of ELBARA-II is narrowed to the protected part 1.400 GHz to 1.427 GHz of the L-band (1–2 GHz) and split into a lower- and an upper sideband allowing for detection of RFI within the protected band. Raw-data (voltages) are sampled at 800 Hz to allow detection of non-thermal RFI from Kurtosis analysis, or by using the more sophisticated approach explained in Naderpour et al., 2017a. Total integration-time of each measurement was 3 s. A matched 50 Ω Resistive noise Source (RS) and an Active Cold Source (ACS) are used as internal references to achieve calibrated antenna temperatures. The noise temperature of the RS corresponds to its physical temperature T_{RS}, at which the instrument is stabilized. Noise temperature of the ACS is calculated from radiometer raw-data measured for the RS and toward the sky of brightness T_{Sky} simulated with the model presented in Pellarin et al., 2003. Thermal noise of antenna feed-cables is compensated in antenna temperatures. Resulting accuracy and sensitivity of antenna temperatures is at least ± 1 K and 0.1 K, respectively, as is demonstrated in Schwank et al., 2012. The antenna connected to the ELBARA-II radiometer is a dual-polarization Pickett horn (Pickett et al., 1984) with a FoV of ∼ ± 8.8° at −6 dB sensitivity relative to boresight. This relatively narrow antenna-beam allows interpreting antenna temperature as brightness temperature of the observed scene falling within the polar-angle ∼ ± 8.8° around the antenna boresight. Polarization cross-talk caused by emission of facets at different polar-angles within the sensitive FoV can be neglected unlike measurements performed with the smaller ELBARA-II antenna of an approximately twice as large FoV (Naderpour et al., 2020).

2.3.2. SMOS brightness temperatures

SMOS is an Earth observation mission of ESA and the Centre National d'Etudes Spatiales (CNES) that provides multi-angular fully polarized brightness temperatures at L-band (1.4 GHz) since 2010. The main objective of SMOS, over land, is surface soil moisture estimation (Kerr et al., 2001; Kerr et al., 2010); whereas simultaneously retrieved L-VOD was given lower priority at the beginning of the SMOS operational phase. However, SMOS L-VOD has been significantly improved over time (Rahmoune et al., 2013; Vittucci et al., 2016), and recently gained interest as it provides information on AGB (Saatchi et al., 2011) and the related vegetation carbon stocks (Brandt et al., 2018). L-VOD is mostly studied over tropical forests (Chaparro et al., 2019), with few studies focused over boreal forests in high latitudes (Roy et al., 2020).

Section 4.2 of this study investigates the temperature dependence $\tau_{\mathrm{C}}(T_{\mathrm{C}})$ of SMOS-based L-VOD over the forest-dominated "Sodankylä grid cell" (Section 2.1). The operational SMOS L-VOD product is not used in our investigation to facilitate control over the retrieval of τ_{C}, for instance, in terms of: i) Choosing the source of vegetation- and ground temperature, and ii) avoiding guiding-terms (Kerr et al., 2020) in the Cost-Function (*CF*) minimized in the retrieval. Instead, the simple approach outlined in Section 3.2 is used to retrieve L-VOD and effective Ground permittivity ($\tau_{\mathrm{C}}, \varepsilon_{\mathrm{G}}$) from multi-angle SMOS Level-3 Brightness Temperatures (L3TB). The used Centre Aval du Traitement des Données SMOS (CATDS) L3TB version 300 are Top-of-Atmosphere (T-A) brightness temperatures $T_{\mathrm{B,SMOS,T\text{-}A}}{}^{p,\theta}$ at horizontal and vertical polarization $p = \{\mathrm{H}, \mathrm{V}\}$ averaged per bin $\{0-5, 5-10, \ldots, 55-60\}^{\circ}$ of maximal 12 observation angles $\theta = \{2.5^{\circ}, 7.5^{\circ}, 12.5^{\circ}, 17.5^{\circ}, 22.5^{\circ}, 27.5^{\circ}, 32.5^{\circ}, 37.5^{\circ}, 42.5^{\circ}, 47.5^{\circ}, 52.5^{\circ}, 57.5^{\circ}\}$ relative to nadir at the ground. SMOS CATDS L3TB come as NetCDF files projected on the Equal-Area Scalable Earth (EASE) grid version 2 with grid-cell area of ∼ 625 m^2 corresponding to the spatial resolution of ∼ 25 km (Al Bitar et al., 2017).

3. Methodology

Fig. 2(a) sketches the measurement setup of ELBARA-II acquiring downwelling, Below-Canopy (B-C) brightness temperatures $T^{p}_{\mathrm{B,B\text{-}C}}$ at polarization $p = \{\mathrm{H}, \mathrm{V}\}$ and the zenith angle $\theta_{\mathrm{Zen}} = 50^{\circ}$ (Section 2.3.1). Fig. 2(b) sketches the SMOS satellite measuring Top-of-Atmosphere (T-A) brightness temperatures $T^{p,\theta}_{\mathrm{B,SMOS,T\text{-}A}}$ at nadir observation angles in the range $\theta = 2.5^{\circ}$ to 57.5° (Section 2.3.2).

3.1. L-VOD from below-canopy ELBARA-II brightness temperatures

One part of this study investigates temperature dependence $\tau_{\mathrm{C}}(T_{\mathrm{C}})$ of tree Canopy's L-VOD at FMI-ARC derived from close-range $T^{p}_{\mathrm{B,B\text{-}C}}$ (Section 2.3.1) measured at $\theta_{\mathrm{Zen}} = 50^{\circ}$ (Fig. 1(c–e)). Canopy L-VOD τ^{p}_{C} at zenith ($\theta_{\mathrm{Zen}} = 0^{\circ}$) is related to Canopy transmissivity t^{p}_{C} along the propagation path for $\theta_{\mathrm{Zen}} = 50^{\circ}$ via Beer's law:

$$t^{p}_{\mathrm{C}} \equiv \exp(-\tau^{p}_{\mathrm{C}}/\cos\theta_{\mathrm{Zen}}) \tag{1}$$

Transmissivity t^{p}_{C} defines emissivity $1 - t^{p}_{\mathrm{C}}$ provided that the Canopy is in thermal equilibrium. Downwelling $T^{p}_{\mathrm{B,B\text{-}C}}$ below the tree Canopy of temperature T_{C} is expressed as canopy thermal emission $T_{\mathrm{C}} \cdot (1 - t^{p}_{\mathrm{C}})$ in downward direction, plus downwelling sky radiance attenuated by the canopy given by $T_{\mathrm{Sky}} \cdot t^{p}_{\mathrm{C}}$ (Fig. 2(a)):

$$T^{p}_{\mathrm{B,B-C}} = T_{\mathrm{C}} \cdot (1 - t^{p}_{\mathrm{C}}) + T_{\mathrm{Sky}} \cdot t^{p}_{\mathrm{C}} \tag{2}$$

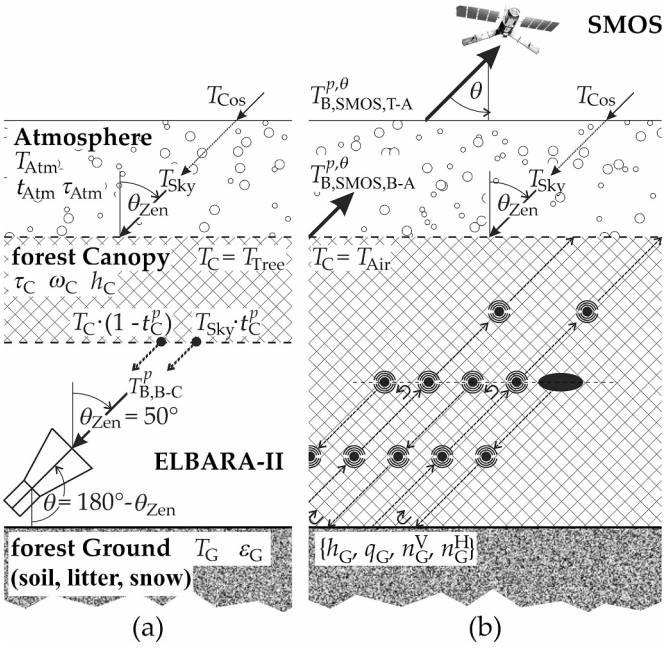

Fig. 2. Measurement configurations of: (a) the Below-Canopy (B-C) ELBARA-II L-band radiometer, and (b) the SMOS satellite. Radiative components of the emission models used to achieve L-VOD τ_C from close-range $T^p_{B,B\text{-}C}$ at $\theta_{Zen} = 50°$ (Sections 3.1 and 4.1) and to achieve L-VOD τ_C from SMOS multi-angle $T_{B,SMOS,T\text{-}A}{}^{p,\theta}$ (Sections 3.2 and 4.2) are indicated. Symbols are explained in the text.

The radiative contribution in $T^p_{B,B\text{-}C}$ caused by upwelling forest-ground emission with adjacent downward reflection by the canopy can be ignored (Mätzler, 1994). Solving Eq. (2) for t^p_C and using definition (1) yields L-VOD τ^p_C at zenith expressed by $T^p_{B,B\text{-}C}$ measured at θ_{Zen} and Canopy temperature $T_C = T_{Tree}$ represented by in-situ Tree skin-temperature (Section 2.2):

$$\tau^p_C = \cos\theta_{Zen} \cdot \mathrm{Ln}\left(\frac{T_C - T_{Sky}}{T_C - T^p_{B,B-C}}\right) \tag{3}$$

In analogy to Eq. (2), downwelling Sky radiance T_{Sky} above the canopy is:

$$T_{Sky} = T_{Atm} \cdot (1 - t_{Atm}) + T_{Cos} \cdot t_{Atm} \tag{4}$$

Cosmic background radiation is considered as $T_{Cos} = 2.7$ K. Transmissivity t_{Atm} and equivalent temperature T_{Atm} of the atmosphere are defined as (Pellarin et al., 2003):

$$\begin{aligned} T_{Atm} &= \exp(4.927 + 0.002195 \cdot T_{Air}) \\ t_{Atm} &= \exp(-\tau_{Atm}/\cos\theta_{Zen}) \\ \tau_{Atm} &= \exp(-3.926 - 0.2211 \cdot Z - 0.00369 \cdot T_{Air}) \end{aligned} \tag{5}$$

These empirical equations involve the altitude Z [km] of the radiometer above sea level ($Z = 0.191$ km for FMI-ARC), and Air temperature [K] at 2 m above ground represented by in-situ T_{Air} (Section 2.2).

3.2. L-VOD from SMOS brightness temperatures

L-VOD and effective Ground permittivity (τ_C, ε_G) are retrieved simultaneously from multi-angle SMOS Top-of-Atmosphere (T-A) L3TB $T^{p,\theta}_{B,SMOS,T\text{-}A}$ (Section 2.3.2). In a first step $T^{p,\theta}_{B,SMOS,T\text{-}A}$ are translated to Below-Atmosphere (B-A) $T^{p,\theta}_{B,SMOS,B\text{-}A}$ using the method described in Houtz et al., 2019:

$$T^{p,\theta}_{B,SMOS,B-A} = \frac{T^{p,\theta}_{B,SMOS,T-A} - T_{Atm} \cdot (1 - t_{Atm})}{t_{Atm}} \tag{6}$$

Atmosphere equivalent temperature T_{Atm} and transmissivity t_{Atm} are computed with Eq. (5), considering the replacement $\theta_{Zen} \longmapsto \theta$. For SMOS AM (~ 06:00) and PM (~ 18:00) overpasses T_{Air} is represented by in-situ Air temperatures (Section 2.2) averaged over the day-hours 05:00 – 07:00 and 17:00 – 19:00, respectively.

Finally, a two-parameter retrieval (τ_C, ε_G) is achieved by minimizing the Cost-Function (*CF*) expressing the sum of squared differences between SMOS $T^{p,\theta}_{B,SMOS,B\text{-}A}$ and $T^{p,\theta}_{B,2S}$ simulated with the Two-Stream Emission Model (2S EM) (Schwank et al., 2018):

$$CF(\tau^*_C \varepsilon^*_G) = \sum_{\theta,p} \left(T^{p,\theta}_{B,SMOS,B-A} - T^{p,\theta}_{B,2S}(\tau^*_C \varepsilon^*_G)\right)^2 \tag{7}$$

The values $\tau_C{}^* = \tau_C$ and $\varepsilon_G{}^* = \varepsilon_G$ which minimize *CF* are considered as successful retrievals if they fall into meaningful ranges, here considered as $0 \le \tau_C{}^* \le 2$ and $1 \le \varepsilon_G{}^* \le 30$. Numerical minimization of *CF* ($\tau_C{}^*, \varepsilon_G{}^*$) is done with a global nonlinear minimization algorithm employing "simulated annealing" (Carr, 2021; Kirkpatrick et al., 1983). The above *CF* does not incorporate any guiding-term, in contrast to the case of the operational SMOS algorithm (Kerr et al., 2020). As mentioned, avoiding guiding-terms, that can impact retrievals, poses one of the reasons for retrieving (τ_C, ε_G) from SMOS L3TB rather than using the SMOS operational or the SMOS-IC L-VOD product.

Ascending and descending SMOS orbits with respective local overpasses at ~ 06:00 AM and ~ 18:00 PM are treated separately to compute associated AM and PM retrieval pairs. The only two constraints applied to the retrievals are adopted from the SMOS-IC algorithm (Fernandez-Moran et al., 2017): i) At least 7 of the maximal 12 elevation angles θ included in a SMOS L3TB angular-scan must be available; ii) Root Mean Squared Difference (RMSD) between an optimally modeled scan-set $T^{p,\theta}_{B,2S}$ and the respective SMOS $T^{p,\theta}_{B,SMOS,B\text{-}A}$ must be < 10 K.

The 2S EM used to simulate $T^{p,\theta}_{B,2S}$ is explained in detail in Schwank et al., 2018. The recent study Li et al., 2020 demonstrates that soil moisture and L-VOD retrieved with the SMOS-IC algorithm (Fernandez-Moran et al., 2017) running with the "conventional" Tau-Omega (TO) or the 2S EM are very similar. Over dense vegetation areas, slightly lower unbiased RMSD between in-situ and retrieved soil moisture are observed with 2S EM. Fig. 2(b) sketches the concept of the employed 2S EM, which considers multiple scattering within the canopy as well as multiple reflections between the canopy layer and the ground. The detailed 2S EM equations are provided in Frappart et al., 2020; Li et al., 2020; Schwank et al., 2018. However, for the sake of traceability of the presented SMOS-based retrievals (τ_C, ε_G), the values of the constant 2S EM parameters are provided. Single scattering-albedo is considered as $\omega_{2S} \simeq 0.094$ corresponding to its TO-equivalent $\omega_{TO} \simeq 0.061$ (Schwank et al., 2018). HQN-parameters used to simulate reflectivity of the rough Ground are $\{h_G, q_G, n^V_G, n^H_G\} = \{0.2952, 0, -0.9978, 0.923\}$ (Wigneron et al., 2007; Wigneron et al., 2001). These values correspond with the ones considered in SMOS-IC for the "Sodankylä grid cell". They are computed by linear weighting of the parameter-values associated with the land-classes according to their areal fractions (Section 2.1) in the forest dominated "Sodankylä grid cell" (Fernandez-Moran et al., 2017).

L-band brightness temperatures are impacted by organic litter and snow at the ground via refraction, impedance matching and absorption (Lemmetyinen et al., 2016a; Schwank et al., 2014). Nonetheless, the 2S EM configuration used to retrieve (τ_C, ε_G) from SMOS L3TB (Section 2.3.2) includes neither a litter layer nor a snow layer. Instead, the ground is understood as soil covered with organic litter and possibly snow (Fig. 2). Accordingly, ε_G, simultaneously retrieved with τ_C, reflects the effective permittivity of the Ground compartment.

In-situ Air- and Soil temperatures T_{Air} and $T_{Soil,5cm}$, $T_{Soil,30cm}$ (Section 2.2) averaged over the day-hours 05:00 – 07:00 and 17:00 – 19:00 are used to simulate $T^{p,\theta}_{B,2S}$ representative of SMOS AM (~ 06:00) and PM (~ 18:00) overpasses, respectively. It is recalled that the same 2-h averages of in-situ T_{Air} are used in the translation $T^{p,\theta}_{B,SMOS,T\text{-}A} \mapsto T_{B,SMOS,B\text{-}A}{}^{p,\theta}$ and to compute T_{Sky}. Likewise, effective Ground temperatures T_G during AM and PM overpasses are computed empirically from in-situ $T_{Soil,5cm}$ and $T_{Soil,30cm}$ (Choudhury et al., 1982):

$$T_G = T_{Soil,30cm} + C\cdot\left(T_{Soil,5cm} - T_{Soil,30cm}\right) \text{ with } C = 0.246 \quad (8)$$

For accurate calculation of T_G, the ground temperature-profile $T(z)$ should be integrated over depth z considering the profile $\alpha(z) = 4\pi/\lambda\cdot \mathrm{Im}\sqrt{\varepsilon_G(z)}$ of the microwave absorption coefficient defined by the profile $\varepsilon_G(z)$ of complex Ground permittivity $\varepsilon_G = \varepsilon'_G + i\cdot\varepsilon''_G$ (Chanzy et al., 1997):

$$T_G = \frac{1}{\cos\theta}\int_0^\infty T(z)\cdot\alpha(z)\cdot\exp\left(-\frac{B(z)}{\cos\theta}\right)\cdot dz$$
$$B(z) = \int_0^z \alpha(z')\cdot dz' \quad (9)$$

Accuracy of the empirical approach (8) depends on thermal- and microwave properties of the ground, which can include soil layers, organic litter, and a layered, moist snowpack atop as is indicated in Fig. 2. However, due to lack of knowledge on these properties, and the small impact of uncertainty in T_G on simulated $T^{p,\theta}_{B,2S}$, Eq. (8) is used for estimation of effective Ground temperature T_G.

3.3. L-VOD model

A novel L-VOD model is developed to simulate τ_C for comparison with L-VOD derived from single-angle, close-range brightness temperatures $T^p_{B,B\text{-}C}$ and multi-angle SMOS L3TB $T^{p,\theta}_{B,SMOS,T\text{-}A}$. Where possible, it uses quantifiable forest parameters as inputs. The model explains EM-induced reasons of temperature dependence $\tau_C(T_C)$ of an unfrozen canopy ($T_C > 0$ °C) by means of the temperature dependence $\varepsilon_{Water}(T_C)$ of liquid-water permittivity. Temperature dependence of a freezing canopy ($T_C \lesssim 0$ °C) is modeled via the reduction of vegetation-internal liquid-water (wood sap-water) because of freezing.

Branches are most determinative for L-VOD of a forest Canopy (Ferrazzoli and Guerriero, 1996). Henceforth, they are referred to as "Small Canopy Constituents" (SCC). Thus, L-band radiative transfer of the canopy is mimicked by a cloud of homogeneously and isotopically distributed SCC. Each SCC is represented by a highly prolate rotation-symmetric ellipsoidal dielectric inclusion embedded in air. The resulting effective complex permittivity $\varepsilon_C = \varepsilon'_C + i\cdot\varepsilon''_C$ of the Canopy layer is simulated with the respective Maxwell Garnet mixing rule (Sihvola, 1999). It determines the canopy layer's absorption coefficient α_C, and hence its L-VOD τ_C. Volume scattering within the canopy layer plays a minor role at L-band (Schwank et al., 2018). Therefore, it is neglected to keep the L-VOD model simple and practically applicable. Also for practical reasons, effects of bound water present in vegetation is ignored (Ulaby and El-Rayes, 1987). Section 3.3.1 describes the L-VOD model equations, example model evaluations and sensitivities are presented in Section 3.3.2.

3.3.1. L-VOD model equations

Nadir optical depth τ_C [−] of a homogenous and isotropic vegetation Canopy of height h_C [m] is defined as:

$$\tau_C \equiv \alpha_C\cdot h_C \quad (10)$$

The power absorption coefficient α_C [m^{-1}] within the Canopy layer is computed from the Canopy layer's effective permittivity $\varepsilon_C = \varepsilon'_C + i\cdot\varepsilon''_C$ [−] at wavelength $\lambda = c/f$ [m] (Mätzler, 2006) ($c \simeq 3\cdot 10^8$ m s^{-1} and frequency f [Hz]):

$$\alpha_C = 4\pi\Big/\lambda\cdot\mathrm{Im}\sqrt{\varepsilon_C} = 4\pi\Big/\lambda\cdot\sqrt{\varepsilon'_C\Big/2\cdot\left(\sqrt{1+(\varepsilon''_C/\varepsilon'_C)^2}-1\right)} \quad (11)$$

Effective permittivity ε_C is computed with an approximate Maxwell Garnett mixing rule applicable for randomly oriented highly prolate and rotation-symmetric ellipsoidal inclusions:

$$\varepsilon_C = \varepsilon_{Air} + \frac{(\varepsilon_{Wood}-\varepsilon_{Air})\cdot(\varepsilon_{Wood}+5\cdot\varepsilon_{Air})\cdot\nu_{SCC}}{3\cdot(\varepsilon_{Wood}+\varepsilon_{Air}) - 2\cdot(\varepsilon_{Wood}-\varepsilon_{Air})\cdot\nu_{SCC}} \quad (12)$$

As is outlined in the Appendix, the expression above is derived from further specifying the Maxwell Garnett mixing rule developed in section 9.3.2 in Sihvola, 1999 for randomly oriented ellipsoidal inclusions of any axial ratio.

The volume fraction of SCC $\nu_{SCC} \equiv V_{SCC}/V_C$ is defined as the ratio between the volume V_{SCC} occupied by SCC and the total Canopy-volume V_C. We define A as the unit area, and $\rho_{Wood,Dry}$ as the mass-density of dry wood accounting for all mass-dominant canopy constituents (trunks, branches). V_{SCC} and V_C are then related to the respective Column-Masses $CM_{SCC,Dry} = V_{SCC}\cdot\rho_{Wood,Dry}/A$ and $CM_{Bulk\text{-}Wood,Dry} = V_C\cdot\rho_{Wood,Dry}/A$. Consequently, ν_{SCC} can be expressed by means of Column-Masses:

$$\nu_{SCC} \equiv V_{SCC}/V_C = CM_{SCC,Dry}/CM_{Bulk-Wood,Dry} \quad (13)$$

$CM_{Bulk\text{-}Wood,Dry}$ represents the Column-Mass of a pile of dry bulk-wood of mass-density $\rho_{Wood,Dry}$ and height h_C:

$$CM_{Bulk-Wood,Dry} = V_C\cdot\rho_{Wood,Dry}/A = \rho_{Wood,Dry}\cdot h_C \quad (14)$$

Now, we define the gravimetric fraction m_{SCC} of SCC as the ratio between $CM_{SCC,Dry}$ of only the Dry SCC and the Column-Mass $CM_{C,Dry}$ of the entire Dry Canopy:

$$m_{SCC} \equiv CM_{SCC,Dry}/CM_{C,Dry} \quad (15)$$

Using Eqs. (14) and (15) in Eq. (13) yields the volume fraction ν_{SCC} of SCC in the total canopy-volume V_C as it is required in the Maxwell Garnett mixing rule (12):

$$\nu_{SCC} = \frac{CM_{C,Dry}\cdot m_{SCC}}{h_C\cdot\rho_{Wood,Dry}} \quad (16)$$

The only remaining parameter used in Eq. (12) to compute ε_C is the permittivity ε_{Wood} of fresh Wood. The latter is modeled with a linear three-phase dielectric mixing model (a special case of the power-law model, see e.g. section 9.4.1 in Sihvola, 1999) considering: i) The H2O-phase consisting of liquid water and ice; ii) the Wood-Cell-phase consisting of the Wood-Cell material; and iii) the Air-phase. Permittivities of these three dielectric phases are ε_{H2O}, $\varepsilon_{Wood\text{-}Cells}$, and $\varepsilon_{Air} = 1$. Associated volume fractions are expressed by fresh-wood porosity por [−] and the volume-fraction ν_{H20} [−] of the H2O-phase:

$$\varepsilon_{Wood} = \nu_{H20}\cdot\varepsilon_{H2O} + (1-por)\cdot\varepsilon_{Wood-Cells} + (por-\nu_{H20})\cdot\varepsilon_{Air} \quad (17)$$

The volume fraction ν_{H20} of the H2O-phase follows from the gravimetric water-content WC_{Wood} [−] of fresh Wood and the mass-densities $\rho_{Water} = 1000$ kg m^{-3} and $\rho_{Wood,Dry}$ [kg m^{-3}] of Water and Dry-Wood, respectively. If shrinkage or swelling of wood is ignored, ν_{H20} reads:

$$\nu_{H2O} = WC_{Wood}\cdot\rho_{Wood,Dry}/\rho_{Water} \quad (18)$$

Permittivity ε_{H2O} of the H2O-phase is represented by another linear dielectric mixing model considering the liquid-water- and the ice phase with respective permittivities ε_{Water} and ε_{Ice}, and associated volume fractions ν_{Water}, and $\nu_{Ice} = 1 - \nu_{Water}$:

$$\varepsilon_{H2O} = \nu_{Water}\cdot\varepsilon_{Water} + (1-\nu_{Water})\cdot\varepsilon_{Ice} \quad (19)$$

Complex permittivity $\varepsilon_{Water} = \varepsilon'_{Water} + i\cdot\varepsilon''_{Water}$ of water at frequency f, temperature $T = T_C$ and of salinity S_{Water} [ppt] is computed with the model described in Klein and Swift, 1977. Complex permittivity $\varepsilon_{Ice} = \varepsilon'_{Ice} + i\cdot\varepsilon''_{Ice}$ of Ice at f [GHz] and $T = T_C$ [K] is computed with the approach implemented in the Microwave Emission Model for Layered Snowpacks (MEMLS) (Mätzler, 1996, updated 2004; Mätzler and Wiesmann, 2012; Wiesmann and Mätzler, 1999). According to Mätzler, 1987 the real part ε'_{Ice} can be considered as frequency-independent from 10 MHz to 300 GHz with a slight dependency on temperature and the maximum $\varepsilon'_{Ice} = 3.1884$ at $T = 0$ °C:

$$\varepsilon'_{Ice} = 3.1884 + 9.1\cdot10^{-4}\cdot(T - 273\text{ K}) \text{ for } 243\text{ K} \le T \le 273\text{ K} \quad (20)$$

For non-saline ice, considered in our L-VOD model, the imaginary

part $\varepsilon''_{\mathrm{Ice}}$ is simulated as (Mätzler, 2006):

$$\varepsilon''_{\mathrm{Ice}} = \alpha/f + \beta \cdot f$$

$$\alpha = (0.00504 + 0.0062 \cdot \Theta) \cdot \exp(-22.1 \cdot \Theta) \text{ with } \Theta = 300\ \mathrm{K}/T - 1$$

$$\beta = \frac{B_1}{T} \cdot \frac{\exp(b/T)}{(\exp(b/T) - 1)^2} + B_2 \cdot f^2 + \exp(-9.963 + 0.0372 \cdot (T - 273.16\ \mathrm{K}))$$

$$\text{with } B_1 = 0.0207\ \mathrm{K\ GHz^{-1}}, B_2 = 1.16 \cdot 10^{-11}\ \mathrm{GHz^{-3}}, b = 335\ \mathrm{K} \quad (21)$$

Eqs. (17)–(21) represent permittivity $\varepsilon_{\mathrm{Wood}} = \varepsilon'_{\mathrm{Wood}} + \mathrm{i} \cdot \varepsilon''_{\mathrm{Wood}}$ of fresh Wood as function of temperature $T = T_{\mathrm{C}}$, fresh-wood porosity *por*, Water salinity S_{Water}, and the Volume-fraction ν_{Water} of liquid water contained in the H2O-phase.

As mentioned above, permittivity $\varepsilon_{\mathrm{H2O}}$ of the H2O-phase is represented by the linear two-phase dielectric mixing model (Eq. (19)) including the volumetric fractions ν_{Water} and $\nu_{\mathrm{Ice}} = 1 - \nu_{\mathrm{Water}}$ of liquid Water and Ice. It is the fractions of liquid water and ice that initiates $\varepsilon_{\mathrm{Wood}}$ undergoing a change from unfrozen to frozen or vice versa. Accordingly, ν_{Water} is defined as a piece-wise function of Canopy temperature T_{C}:

$$\nu_{\mathrm{Water}}(T_{\mathrm{C}}) = \begin{cases} 1 & \text{for } T_{\mathrm{C}} > 0\,^{\circ}\mathrm{C} \\ \exp(T_{\mathrm{C}}/T_{\mathrm{melt}}) & \text{for } T_{\mathrm{C}} \le 0\,^{\circ}\mathrm{C} \end{cases} \quad (22)$$

The parameter T_{melt} [°C] expresses the rate at which the ice-phase melts. In other words, it defines the temperature below ~ 0 °C at which the liquid-water fraction contained in the H2O-phase is reduced to $\nu_{\mathrm{Water}} = \exp(-1) \simeq 0.37$ from its value $\nu_{\mathrm{Water}} = 1$ for an unfrozen canopy at $T_{\mathrm{C}} > 0$ °C. Admittedly, the physical basis of Eq. (22) is weak and ignores any freeze-thaw hysteresis. Nevertheless, it resembles temperature dependence $\nu_{\mathrm{Water}}(T_{\mathrm{C}})$ of the liquid-water volume fraction reasonably well.

3.3.2. Model sensitivities

Fig. 3 shows intermediate L-VOD model results (namely permittivities $\varepsilon_{\mathrm{H2O}}$, $\varepsilon_{\mathrm{Wood}}$, and power absorption coefficients α_{H2O}, α_{Wood} of the H20-phase and fresh Wood). Fig. 4 shows τ_{C}, the result of the L-VOD model. Values of the model parameters are included in subsequent figures and listed in Table 1, including their meaning and symbols used in the model equations. Following a survey conducted in 2019 $CM_{\mathrm{C,Dry}} = 10\ \mathrm{kg\ m^{-2}}$ and $h_{\mathrm{C}} = 10$ m are representative of the forest stand at the FMI-ARC and the forest in the wider area of Sodankylä (Finland). Wood Dry mass-density $\rho_{\mathrm{Wood,Dry}} = 300\ \mathrm{kg\ m^{-3}}$ and porosity $por = 0.5$ of fresh wood are selected as typical for the prominent biome (Ding et al., 2008). The real part $\varepsilon'_{\mathrm{Wood\text{-}Cells}} = 5.0$ of Wood-Cells permittivity is estimated from measured real parts of fresh-wood permittivity (Olmi et al., 2000) using a dielectric mixing model fed with realistic values of fresh-Wood gravimetric liquid Water-Content $WC_{\mathrm{Wood}} = 0.3\ \mathrm{kg\ kg^{-1}}$ and $por = 0.5$. The gravimetric fraction $m_{\mathrm{SCC}} = 0.3\ \mathrm{kg\ kg^{-1}}$ of SCC was estimated from visual observations.

Fig. 3(a) shows simulated temperature dependence of real- (blue) and imaginary parts (red) of permittivity $\varepsilon_{\mathrm{H2O}}$ of the H2O-phase including ice and/or liquid water (Eq. (19)) of respective temperature dependent volume fractions $\nu_{\mathrm{Ice}} = 1 - \nu_{\mathrm{Water}}$ and ν_{Water} (Eq. (22)). Temperature dependence of the absorption coefficient α_{H2O} is shown with green lines. Fig. 3(b) shows simulated fresh-Wood permittivity $\varepsilon_{\mathrm{Wood}}$ and respective absorption coefficients α_{Wood}. Lines of the same color are for salinities $S_{\mathrm{Water}} = \{0, 2, 4\}$ ppt of the liquid-water phase of permittivity $\varepsilon_{\mathrm{Water}}$ simulated with the model developed by Klein and Swift, 1977. The simulations cover the range $-15\ ^{\circ}\mathrm{C} \le T_{\mathrm{C}} \le 30\ ^{\circ}\mathrm{C}$, and assume Canopy temperature T_{C} for all dielectric phases of SCC (branches).

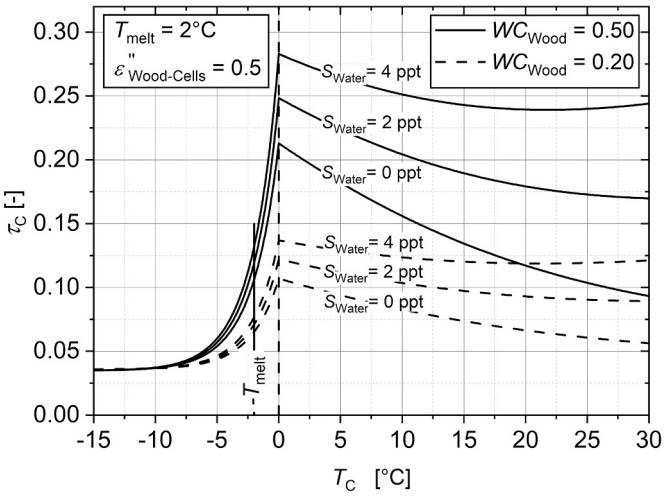

Fig. 4. Simulated temperature dependence $\tau_{\mathrm{C}}(T_{\mathrm{C}})$ of L-VOD. Quantitative information on τ_{C} temperature sensitivity at $T_{\mathrm{C}} = +0$ °C is provided in Table 2. Values of used model parameters are indicated and listed in Table 1.

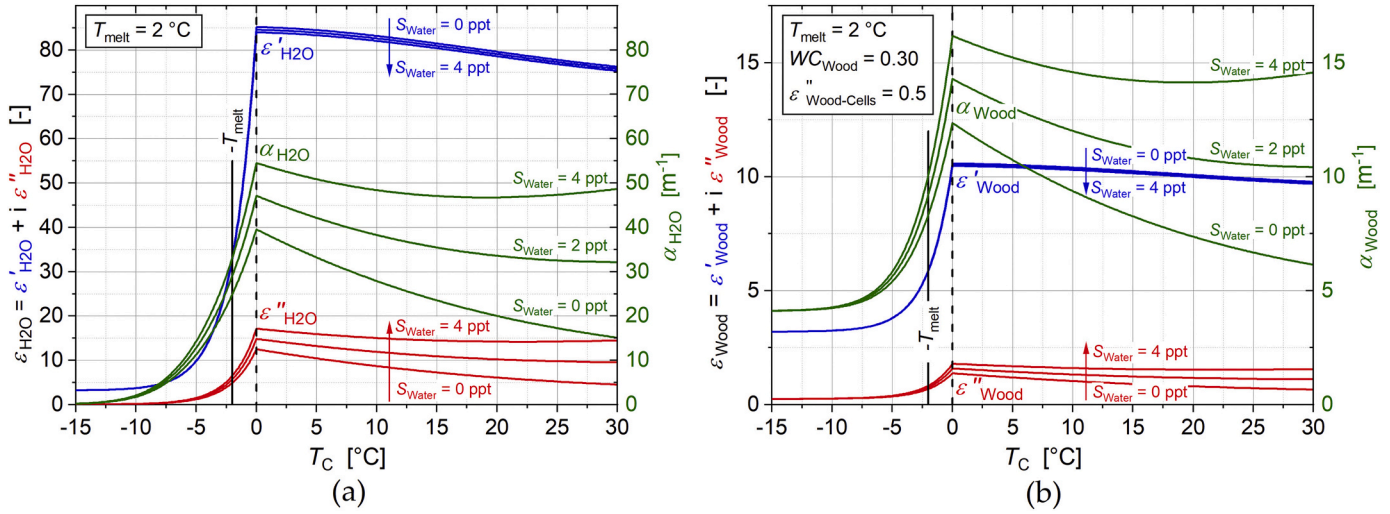

Fig. 3. (a) Simulated temperature dependence of permittivity $\varepsilon_{\mathrm{H2O}} = \varepsilon'_{\mathrm{H2O}} + \mathrm{i} \cdot \varepsilon''_{\mathrm{H2O}}$ and power absorption coefficient α_{H2O} of the H2O-phase (ice and/or liquid water). (b) Simulated temperature dependence of $\varepsilon_{\mathrm{Wood}} = \varepsilon'_{\mathrm{Wood}} + \mathrm{i} \cdot \varepsilon''_{\mathrm{Wood}}$ and α_{Wood} of fresh-Wood of gravimetric liquid Water-Content WC_{Wood}. Values of used model parameters are indicated and listed in Table 1.

Table 1
Symbols of L-VOD model parameters and their meanings. Values are either provided here or indicated in subsequent figures if the parameter is optimized (opt.) to match experimental L-VOD τ_C with simulations.

Symbol	Meaning	Value
$CM_{C,Dry}$	Column-Mass of Dry Canopy	10 kg m^{-2}
h_C	Canopy height	10 m
m_{SCC}	gravimetric fraction of Small Canopy Constituents (SCC)	0.3 kg kg^{-1}
$\rho_{Wood,Dry}$	Dry mass-density of Wood	300 kg m^{-3}
por	Porosity of fresh wood	0.5
$\varepsilon'_{Wood\text{-}Cells}$	real part of permittivity of Wood-Cells	5.0
ρ_{Water}	mass-density of liquid Water	1000 kg m^{-3}
ε_{Air}	permittivity of Air	1.0
f	frequency of electromagnetic wave	1.4 GHz
T_C	Temperature of vegetation Canopy	obs. T_{Air} or T_{Tree}
WC_{Wood}	fresh-Wood gravimetric liquid Water-Content	0.3 kg kg^{-1} / (opt.)
S_{Water}	Salinity of vegetation liquid-Water (sap-water)	{0, 2, 4} ppt / (opt.)
T_{melt}	H2O-phase melt parameter	2 °C / (opt.)
$\varepsilon''_{Wood\text{-}Cells}$	imaginary part of permittivity of Wood-Cells	0.5 / (opt.)

The first obvious perception from Fig. 3(a) is that real and imaginary parts of $\varepsilon_{H2O} = \varepsilon'_{H2O} + i \cdot \varepsilon''_{H2O}$ are maximal at the melting point $T_C = 0$ °C. With decreasing temperature $T_C < 0$ °C, both ε'_{H2O} and ε''_{H2O} decrease distinctly as the result of the gradual change of the aggregate state of the H2O-phase from pure liquid-water to ice.

At $T_C \ll -T_{melt}$ the H2O-phase consists of almost exclusively pure ice ($\nu_{Water} \to 0$, $\nu_{Ice} \to 1$). Accordingly, permittivity $\varepsilon_{H2O}(T_C \ll -T_{melt})$ of the deeply frozen H2O-phase approaches permittivity $\varepsilon_{Ice} = \varepsilon'_{Ice} + i \cdot \varepsilon''_{Ice} \simeq 3.175 + i \cdot 3.710 \cdot 10^{-4}$ of Ice, which is much smaller compared to $\varepsilon_{Water} = \varepsilon'_{Water} + i \cdot \varepsilon''_{Water} \simeq 85.192 + i \cdot 12.487$ of liquid water of $S_{Water} = 0$ ppt at $T_C = 0$ °C. For $T_C > 0$ °C, the H2O-phase consists of exclusively liquid water ($\nu_{Water} = 1$ and $\nu_{Ice} = 0$). Hence, $\varepsilon_{H2O}(T_C)$ corresponds with the temperature sensitivity $\varepsilon_{Water}(T_C)$ of liquid water for salinity $S_{Water} = \{0, 2, 4\}$ ppt. Simulated real parts $\varepsilon'_{H2O} = \varepsilon'_{Water}$ are slightly decreasing with increasing $S_{Water} = \{0, 2, 4\}$ ppt, while imaginary parts $\varepsilon''_{H2O} = \varepsilon''_{Water}$ show opposite and relatively stronger responses. Generally, the impact of S_{Water} on ε_{H2O} is more distinct for $T_C > 0$ °C than for $T_C < 0$ °C. This is because ε_{H2O} is modeled as the dielectric mixture of non-saline ice and liquid water (Eq. (19)) of $S_{Water} \geq 0$ ppt, whereas the liquid phase becomes less impactful with evanescent volumetric liquid-water fraction ($\nu_{Water} \to 0$) for decreasing $T_C < 0$ °C.

In analogy to Eq. (11), the power absorption coefficient of the H2O-phase is computed as $\alpha_{H2O} = 4\pi/\lambda \cdot \mathrm{Im}\sqrt{\varepsilon_{H2O}}$. Naturally, the temperature response $\alpha_{H2O}(T_C)$ bears similarities to $\varepsilon_{H2O}(T_C)$. However, on closer inspection, one can see that with decreasing temperature below 0 °C, α_{H2O} decreases more linearly and hence less distinctly than the real and imaginary parts of ε_{H2O}. With increasing $T_C > 0$ °C, the characteristics of $\alpha_{H2O} = \alpha_{Water}$ responds to water-salinity S_{Water} in two ways: i) Increasing S_{Water} increases α_{H2O}, and ii) temperature sensitivity $\alpha_{H2O}(T_C)$ is most pronounced for pure water ($S_{Water} = 0$ ppt) and it becomes cushioned with increasing $S_{Water} = \{2, 4\}$ ppt.

Fig. 3(b) shows real-parts ε'_{Wood} (blue) and imaginary parts ε''_{Wood} (red) of ε_{Wood}, and power absorption coefficients $\alpha_{Wood} = 4\pi/\lambda \cdot \mathrm{Im}\sqrt{\varepsilon_{Wood}}$ (green). Complex Wood permittivity ε_{Wood} is modeled as the mixture of the air-phase, the wood-cell phase, and the H2O-phase (Eq. (17)). Wood permittivity $\varepsilon_{Wood} = \varepsilon'_{Wood} + i \cdot \varepsilon''_{Wood}$ simulated for $T_C \geq 0$ °C are well comparable with corresponding measured values that can be found in literature (Olmi et al., 2000; Roy et al., 2020).

Consequently, responses of $\varepsilon_{Wood} = \varepsilon'_{Wood} + i \cdot \varepsilon''_{Wood}$ and α_{Wood} to T_C show similarities to the discussed temperature responses of $\varepsilon_{H2O} = \varepsilon'_{H2O} + i \cdot \varepsilon''_{H2O}$ and α_{H2O} of the H2O-phase. However, the two most noticeable differences between the temperature responses of ε_{H2O}, α_{H2O} (Fig. 3(a)) and ε_{Wood}, α_{Wood} (Fig. 3(b)) are: i) For deeply frozen situations ($T_C \ll -T_{melt} \leftrightarrow \nu_{Water} \to 0$, $\nu_{Ice} \to 1$) ε_{H2O} and α_{H2O} approach the low values $\varepsilon_{H2O} \mapsto \varepsilon_{Ice} \simeq 3.175 + i \cdot 3.710 \cdot 10^{-4}$ and $\alpha_{H2O} \mapsto \alpha_{Ice} \simeq 0.006$ m^{-1}. The respective decrease in ε_{Wood} and α_{Wood} as the result of freezing liquid-water are clearly less distinct. This is because permittivity $\varepsilon_{Wood\text{-}Cells} \simeq 5.0 + i \cdot 0.5$ (Table 1) of the Wood-Cell phase is considered as temperature-independent. This imposes a minimum threshold to ε_{Wood} for deeply frozen wood. ii) For unfrozen situations ($T_C > 0$ °C $\leftrightarrow \nu_{Water} = 1$, $\nu_{Ice} = 0$) ε_{Wood} and α_{Wood} are consistently smaller than respective ε_{H2O} and α_{H2O} of the H2O-phase. This is because $\varepsilon_{Air} = 1$ and $\varepsilon_{Wood\text{-}Cells} \simeq 5.0 + i \cdot 0.5$ are much smaller than ε_{Water} of the liquid water contained in wood, and therefore dilute the three-phase dielectric mixing representing ε_{Wood}.

Fig. 4 shows temperature dependence $\tau_C(T_C)$ simulated with the L-VOD model (Section 3.3.1). Like in Fig. 3, the model input parameters provided in Table 1 are used to simulate τ_C for gravimetric liquid Water-Content $WC_{Wood} = 0.20$ (dashed line) and $WC_{Wood} = 0.50$ (solid line) of Wood sap-water of salinities $S_{Water} = \{0, 2, 4\}$ ppt.

The first obvious feature seen in Fig. 4 is the pronounced decrease of L-VOD τ_C when Canopy temperature T_C falls below the melting temperature. Again, this is due to the reduction of liquid water contained in the H20-phase of fresh wood. For $T_C > 0$ °C simulated τ_C increase with increasing WC_{Wood}. In other words, fresh-Wood liquid Water-Content WC_{Wood} has a "positive scaling effect" on τ_C. However, WC_{Wood} is not the only model parameter with an almost proportional "positive scaling effect" on τ_C. For instance, increasing the gravimetric fraction m_{SCC} of Small Canopy Constituents (SCC, branches) linearly increases the volume fraction ν_{SCC} of SCC used in the Maxwell Garnett mixing rule (12) to compute ε_C, that determines α_C, and finally τ_C via Eq. (10). Therefore, doubling the selected value of $m_{SCC} = 0.3$ kg kg^{-1} (Table 1) would almost double simulated τ_C. For similar reasons, Column-Mass of Dry Canopy ($CM_{C,Dry} = 10$ kg m^{-2}) has a "positive scaling effect" on τ_C for $T_C > 0$ °C. In turn, fresh-wood porosity *por* is an example of a L-VOD model parameter exhibiting a "negative scaling effect" on unfrozen τ_C. Choosing half of the value *por* = 0.5 used here (Table 1), increases ε_{Wood} and therefore increases simulated τ_C by approximately 20 %. Canopy height h_C is another example of an L-VOD model parameter with a "negative scaling effect". Although h_C increases L-VOD via $\tau_C \equiv \alpha_C \cdot h_C$ (Eq. (10)), increasing h_C "dilutes" the canopy and poses the dominant effect that ultimately lowers τ_C. The increasing dielectric "dilution" with increasing h_C is reflected by the reduce of ν_{SCC} and consequently ε_C and α_C. However, for now, we shall consider fresh-Wood gravimetric Water-Content WC_{Wood} as the only parameter with a "positive scaling effect" on τ_C simulated for $T_C > 0$ °C. Other parameters, also increasing τ_C, are considered as constants estimated from forest in-situ observations.

In contrast to the "positive scaling effect" of WC_{Wood}, salinity S_{Water} of wood liquid-Water (sap-water) impacts the degree at which $\tau_C(T_C)$ of an unfrozen canopy decreases with increasing T_C. As apparent from Fig. 4 the respective negative gradient $\Delta\tau \equiv d\tau_C/dT_C|_{T_C=+0°C}$ at $T_C = +0$ °C is most pronounced if wood liquid-water is considered as non-saline ($S_{Water} = 0$ ppt), while with $S_{Water} > 0$ ppt the gradient $\Delta\tau$ becomes less negative. For $S_{Water} = 0$ ppt, τ_C decreases steadily with increasing $T_C \geq 0$ °C, while for $S_{Water} = 2$ ppt and $S_{Water} = 4$ ppt the steady decreases of τ_C with increasing T_C are limited to 0 °C $\leq T_C \lesssim 30$ °C and 0 °C $\leq T_C \lesssim 20$ °C, respectively. Table 2 shows gradients $\Delta\tau$ and associated relative

sensitivities defined as $\delta\tau \equiv 100\,\% \cdot \Delta\tau/\tau_C|_{T_C=+0^\circ C}$ for $S_{Water} = \{0, 2, 4\}$ ppt and $WC_{Wood} = \{0.20, 0.50\}$ kg kg^{-1}. As apparent from Fig. 4, S_{Water} also increases the level of τ_C, meaning that S_{Water} also includes a "positive scaling effect" on τ_C. With this understanding S_{Water} impacts τ_C of an unfrozen Canopy partially "orthogonal" as compared to the exclusively "positive scaling effect" associated with WC_{Wood}.

Similar to the qualitatively different ("orthogonal") impacts of $\{WC_{Wood}, S_{Water}\}$ on $\tau_C(T_C)$ for $T_C > 0$ °C, the L-VOD model parameters $\{\varepsilon''_{Wood-Cells}, T_{melt}\}$ impact $\tau_C(T_C)$ simulated for $T_C \lesssim -T_{melt}$ in qualitatively different manners. The melt parameter T_{melt} determines the gradient of the drop in τ_C due to the freezing H2O-phase, while the imaginary part $\varepsilon''_{Wood-Cells}$ of the Wood-Cells material is determinative for the asymptotic minimum of τ_C approached for deeply frozen conditions ($T_C \ll -T_{melt}$). Therefore, $\{\varepsilon''_{Wood-Cells}, T_{melt}\}$ are regarded as "orthogonal" L-VOD model parameters to express their quantitatively different impact on $\tau_C(T_C)$ simulated for a freezing canopy ($T_C < 0$ °C). Overall, the discussed "orthogonalities" of $\{WC_{Wood}, S_{Water}\}$ and $\{\varepsilon''_{Wood-Cells}, T_{melt}\}$ suggest that these parameters are convenient to optimally match simulated $\tau_C(T_C)$ to L-VOD temperature responses derived from close-range (Section 4.1) and SMOS brightness temperatures (Section 4.2).

4. Results and discussions

4.1. L-VOD derived from below-canopy ELBARA-II brightness temperatures

Fig. 5 shows diurnal minimum (blue down-triangles) and maximum (red up-triangles) of in-situ tree skin-temperature T_{Tree} (Section 2.2) for the period of 1 February 2019–30 April 2019. Diurnal minima and maxima of T_{Tree} are used as the baseline information to decide on the time-period most relevant to our research questions about the EM reasons of temperature dependence of L-VOD τ_C: i) What is the change in L-VOD derived from close-range and SMOS L-band brightness temperatures when the forest canopy goes through transitional freeze/thaw states? ii) Is it possible to explain respective experimental temperature responses $\tau_C(T_C)$ by the developed L-VOD model using meaningful values for the model parameters?

The time-frame of periods with most suitable close-range brightness temperatures was limited to 1 February 2019–30 April 2019 (Fig. 5). Aside from technical reasons, the fact that the canopy was mostly snow-free during this period led us to focus on the late-winter to spring period rather than on the autumn to winter period of the same year. In the light of the recalled study goals, snow-free canopy is important because it avoids intermixing between potential effects of wet snow in the canopy and the sole EM temperature response $\tau_C(T_C)$. Furthermore, during the selected periods, 22 March 2019–15 April 2019 and 6 April 2019, forest phenology does not change much. This is another important prerequisite to investigate primarily EM-induced temperature sensitivity $\tau_C(T_C)$ as is reflected by the L-VOD model developed in Section 3.3.

The 4-week study period includes several canopy freeze/thaw cycles, while the 1-day period features a single sequence of frozen-thawed-frozen canopy. The exploration of the 4-week period (Section 4.1.1) provides insight to EM-induced L-VOD temperature responses at time-scales relevant for satellite observations. The 1-day period (Section 4.1.2) is useful to quantify representativeness of satellite-based L-VOD retrievals, which take place at a given local overpass time.

Table 2
Gradients $\Delta\tau \equiv d\tau_C/dT_C|_{T_C=+0^\circ C}$ and relative sensitivities $\delta\tau \equiv 100\,\% \cdot \Delta\tau/\tau_C|_{T_C=+0^\circ C}$ of L-VOD $\tau_C(T_C)$ shown in Fig. 4 at $T_C = +0$ °C.

WC_{Wood} [kg·kg^{-1}]	S_{Water} [ppt]	$\Delta\tau$ [K^{-1}]	$\delta\tau$ [%·K^{-1}]
0.20	0	−0.0028	−2.6209
0.20	2	−0.0023	−1.8639
0.20	4	−0.0018	−1.2909
0.50	0	−0.0066	−3.0929
0.50	2	−0.0054	−2.1543
0.50	4	−0.0042	−1.4699

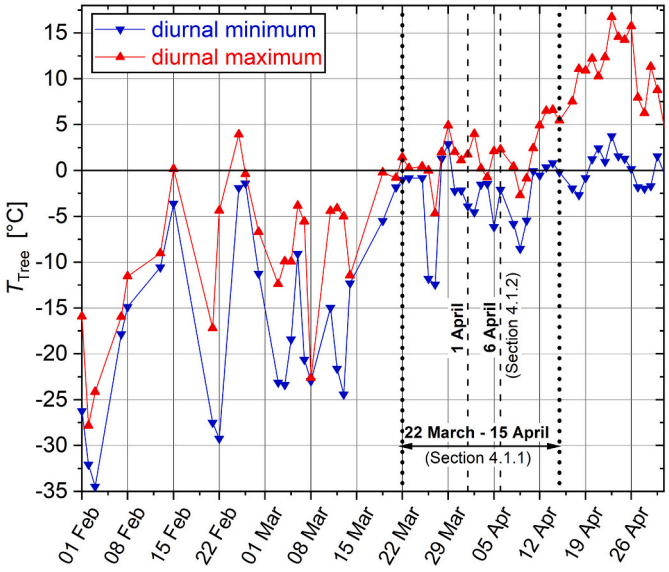

Fig. 5. Diurnal minimum (blue down-triangles) and maximum (red up-triangles) of in-situ tree skin-temperature T_{Tree} (Section 2.2) during the late-winter to spring period of the year 2019. The selected 4-week period (22 March 2019–15 April 2019) and the 1-day period (6 April 2019) analyzed in Sections 4.1.1 and 4.1.2 are indicated.

4.1.1. Four-week period (22 March 2019 – 15 April 2019)

Fig. 6 shows simulated L-VOD, as well as $\tau_C = (\tau_C^H + \tau_C^V)/2$ derived from close-range $T_{B,B-C}^p$, plotted versus Canopy temperature $T_C = T_{Tree}$ represented by in-situ Tree skin-temperature T_{Tree} (Section 2.2). The close-range $T_{B,B-C}^p$, resulting in the shown 260 local-scale L-VODs, are measured at irregular points in time indicated by the color-code.

The most apparent information seen in Fig. 6 is that L-VOD is maximal at $T_C \simeq 0$ °C and becomes smaller for Canopy temperature deviating from $T_C \simeq 0$ °C. This characteristic temperature response corroborates simulated $\tau_C(T_C)$ shown in Fig. 4. The color-codes applied to the experimental τ_C show that highest values (~ 0.22 to ~ 0.25, blue data) are associated with $T_{B,B-C}^p$ measured during the last 5 days (11–15 April 2019) of the selected 4-week period. This is consistent with the fact that $T_C = T_{Tree}$ is consistently above 0 °C during these 5 days (Fig. 5). Likewise, lowest L-VOD values (~ 0.06 to ~ 0.08, orange data) are associated with measurements between 26 and 27 March 2019 with $T_C = T_{Tree}$ always well below 0 °C.

The black line in Fig. 6 shows $\tau_C(T_C)$ simulated with the L-VOD model (Section 3.1). The model parameters $\{WC_{Wood}, S_{Water}\}$ and $\{T_{melt}, \varepsilon''_{Wood-Cells}\}$ are tuned to minimize the RMSD between experimental and simulated L-VOD. A numerical global optimizer is used to find the minimum RMSD. There is only one unique minimum in RMSD for 0 kg kg^{-1} $\leq WC_{Wood} \leq$ 1 kg kg^{-1}, 0 ppt $\leq S_{Water} \leq$ 10 ppt and 0 °C $\leq T_{melt} \leq$ 10 °C, $0 \leq \varepsilon''_{Wood-Cells} \leq 5$ covering at least the meaningful parameter ranges. This corroborates the "orthogonality" of the L-VOD model parameters $\{WC_{Wood}, S_{Water}\}$ and $\{T_{melt}, \varepsilon''_{Wood-Cells}\}$ discussed in Section 3.3.2. Values of the optimized L-VOD model parameters are indicated in Fig. 6, while modeling parameters considered as constants, are listed in Table 1. The minimized RMSD and the resulting coefficient of determination R^2 of the L-VOD model-fit, are indicated in Fig. 6.

The presented result demonstrates that L-VOD's temperature dependence derived from $T_{B,B-C}^p$ is successfully explained by $\tau_C(T_C)$ simulated with the L-VOD model. In other words, the developed L-VOD model includes the driving physical processes to capture the EM-induced temperature response of L-VOD resulting from the temperature response of liquid-water permittivity and the reduction of liquid-water due to

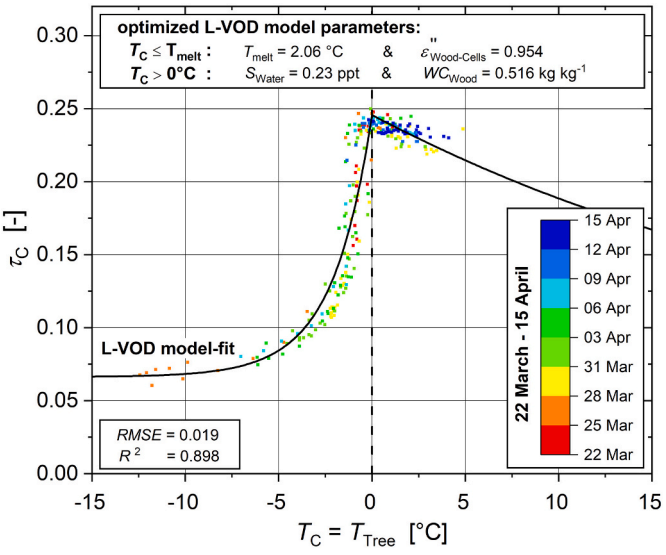

Fig. 6. Scatter-plot of Canopy temperature $T_C = T_{Tree}$ versus L-VOD τ_C derived from close-range $T^p_{B,B\text{-}C}$ at $p = \{H, V\}$ measured at $\theta_{Zen} = 50°$ (Figs. 1(c–e) and 2(b)). Time of measurements are color-coded. The black line is $\tau_C(T_C)$ simulated with the L-VOD model (Section 3.3). Values of optimized model parameter are indicated. Further model parameter considered as constants are listed in Table 1. (For interpretation of the references to color in this figure legend, the reader is referred to the web version of this article.)

freezing. Realization of these processes is of practical relevance for the interpretation of L-VOD. For instance, it means that increased L-VOD around the freezing point is not necessarily the result of increased biomass caused by vegetation growth or rehydration.

Next, we focus on a representative 1-day period (6 April 2019) with $T_C = T_{Tree}$ varying around the melting point, which provides further indication that L-VOD can vary due to EM reasons rather than due to mistakenly adducted changes of forest phenology.

4.1.2. One-day period (6 April 2019)

Fig. 7 shows L-VOD τ_C derived from close-range $T^p_{B,B\text{-}C}$ measured at $\theta_{Zen} = 50°$ (Figs. 1(c–e) and 2(a)) during the 6 April 2019. During this day, 20 undisturbed $T^p_{B,B\text{-}C}$ are available. The upper panel in Fig. 7(a) presents the 1-day time-series of τ^H_C (up-triangles) and τ^V_C (down-triangles) computed from respective $T^H_{B,B\text{-}C}$ and $T^V_{B,B\text{-}C}$ using Eq. (3). Polarization-averaged $\tau_C \equiv (\tau^H_C + \tau^V_C)/2$ are shown with color-coded squares indicating time of measurement. The synchronous time-series of in-situ T_{Tree} and T_{Air} (Section 2.2) are shown in the lower panel of Fig. 7(a). The thawed period 07:00 – 18:00 with $T_{Tree} \simeq T_{Air} \gtrsim 0$ °C is overlayed in light gray. Fig. 7(b) shows $T_C = T_{Tree}$ versus experimental τ_C (color-coded squares) for the 6 April 2019. The black line shows simulated $\tau_C(T_C)$ achieved for the indicated values of optimized "orthogonal" parameters, and the constant parameters listed in Table 1.

Fig. 7(a) shows that τ^H_C at horizontal polarization is systematically larger than τ^V_C at vertical polarization. This is consistent with the study Guglielmetti et al., 2008 performed in a deciduous forest. The finding $\tau^H_C > \tau^V_C$ is explained by anisotropic canopy structure associated with predominantly horizontal orientation of branches (SCC) in most forests (Schwank et al., 2005).

However, polarization-averaged τ_C in Fig. 7(b) follow the expected response with respect to Canopy temperature T_C represented by in-situ Tree skin-temperature T_{Tree}. L-VOD τ_C are minimal when T_C are lowest (~ -1.8 °C at 01:00 and ~ -1.4 °C at 22:00) and L-VOD τ_C are maximal when T_C are close to 0 °C ($\sim +0.9$ °C at 08:00 and $\sim +0.8$ °C at 17:00). On the other hand, during the hours 08:00 to 17:00 with $T_C > 0$ °C, experimental $\tau_C(T_C)$ show the temperature response expected for an unfrozen canopy, meaning that L-VOD decreases from the mentioned two maxima at around $T_C \simeq 0$ °C to its day-time minimum of $\tau_C \simeq 0.23$ at around 11:30 when temperature reaches its maximum. These findings corroborate that strong diurnal variations in L-VOD are most probably not the result of changed forest phenology, but rather due to the discussed EM considerations included in the L-VOD model outlined in Section 3.3.

The discussed qualitative agreement between the L-VOD's theoretical and experimental temperature response enable to represent experimental τ_C of the 6 April 2019 by means of the L-VOD model. The black line in Fig. 7(b) shows $\tau_C(T_C)$ simulated for the indicated optimized L-

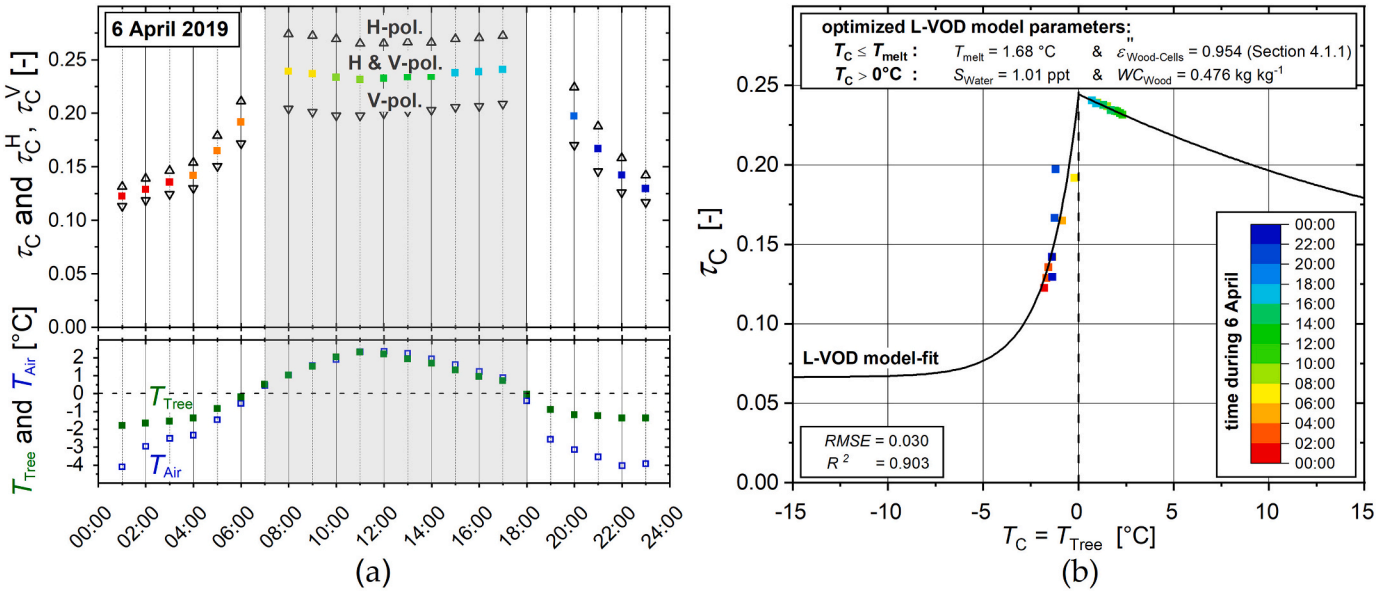

Fig. 7. (a) Upper panel: Time-series during 6 April 2019 of L-VOD derived from close-range $T^p_{B,B\text{-}C}$ measured at $\theta_{Zen} = 50°$ (Figs. 1(c–e) and 2(b)). Up-triangles are τ^H_C derived from $T^H_{B,B\text{-}C}$; down-triangles are τ^V_C derived from $T^V_{B,B\text{-}C}$; colored symbols are polarization-averaged τ_C. (a) Lower panel: Time-series of in-situ Tree- and Air temperature T_{Tree} (green) and T_{Air} (blue). (b) Scatter-plot of $T_C = T_{Tree}$ versus L-VOD τ_C. The black line is $\tau_C(T_C)$ simulated with the L-VOD model (Section 3.3). Values of optimized model parameters are indicated. Further model parameter considered as constants are listed in Table 1. (For interpretation of the references to color in this figure legend, the reader is referred to the web version of this article.)

VOD model parameters and the ones listed in Table 1. As in Section 4.1.1, a global numerical optimization approach is used to compute the values of the three "orthogonal" model parameters T_{melt} and $\{WC_{\mathrm{Wood}}, S_{\mathrm{Water}}\}$ that minimize the RMSD between simulated and experimental L-VOD. Respective RMSD and R^2 of the L-VOD model-fit are indicated in Fig. 7(b). The value of the parameter $\varepsilon''_{\mathrm{Wood\text{-}Cells}} \simeq 0.954$ is taken from the respective optimization performed for the 4-week period (Section 4.1.1). Tuning $\varepsilon''_{\mathrm{Wood\text{-}Cells}}$ for the 1-day period is meaningless because the effect of $\varepsilon''_{\mathrm{Wood\text{-}Cells}}$ is prevailingly on the asymptotic value of τ_C for deeply frozen conditions ($T_C \ll -T_{\mathrm{melt}}$), which is not present on 6 April 2019 with $T_C = T_{\mathrm{Tree}} \gtrsim -1.8$ °C. The findings gained from τ_C derived from close-range $T^p_{B,\mathrm{B\text{-}C}}$ measured on 6 April 2019 are generally valid for days with $T_C = T_{\mathrm{Tree}}$ varying similarly around the melting point of wood sap-water, for instance, on 1 April 2019 with minimum and maximum T_{Tree} of −3.9 °C and + 1.8 °C, respectively (Fig. 5).

The values of the model parameters T_{melt} and $\{WC_{\mathrm{Wood}}, S_{\mathrm{Water}}\}$, optimized to best match local L-VOD of the 4-week period (Fig. 6) and also L-VOD of the 1-day period (Fig. 7(b)), are similar. It is worth noting that consistency between these parameter values stretches over two distinctly different time-scales, whereas the single day, as well as the 4-week period, reflect complementary types of transitional periods. On the one hand, the canopy goes through a single freeze-thaw-freeze cycle during 6 April 2019. On the other hand, the period 22 March 2019 – 15 April 2019 separates the late winter-period, with constantly frozen canopy, from the early summer-period with thawed canopy. Accordingly, consistency between optimized T_{melt} and $\{WC_{\mathrm{Wood}}, S_{\mathrm{Water}}\}$ stands for similar L-VOD temperature responses during the 1-day and the 4-week transitional period. This indicates the possibility to characterize L-VOD temperature response at longer time-scales (4 weeks) from short-term (1-day) observations of L-VOD temperature response, and vice versa.

4.2. L-VOD from SMOS brightness temperatures

The goal of this section is to ascertain whether the EM-induced temperature response seen in the local-scale L-VOD (Section 4.1) is also apparent in τ_C retrieved simultaneous with ε_G from multi-angle SMOS L3TB $T^{p,\theta}_{B,\mathrm{SMOS,T\text{-}A}}$ (Section 3.2) over the "Sodankylä grid cell" (Section 2.3.2). SMOS AM (~ 06:00) and PM (~ 18:00) overpasses, together with associated in-situ ground- and air-temperatures (Section 2.2) are used to achieve AM and PM retrieval-pairs (τ_C, ε_G) for the time-period from 1 February 2019 to 31 May 2019. This period is selected for three reasons: ii) It includes the period from 22 March to 15 April 2019 for which temperature dependence $\tau_C(T_C)$ of L-VOD computed from close-range $T^p_{B,\mathrm{B\text{-}C}}$ are analyzed (Section 4.1.1). ii) Forest phenology is expected to be relatively constant because it is before the growing period. The latter is important to separate EM reasons of L-VOD temperature dependence from impacts of changing forest phenology. iii) Spatio-temporal variability of microwave emission of the forest ground is expected to be relatively small compared to later summer-periods, implying that retrieval crosstalk from ε_G to τ_C is at least relatively constant.

However, quantitative agreement between L-VOD τ_C derived from close-range $T^p_{B,\mathrm{B\text{-}C}}$ (Section 4.1) and τ_C retrieved from SMOS L3TB is not expected for a number of reasons: i) Local τ_C are not necessarily representative of τ_C at the SMOS scale. ii) Local τ_C are determined almost exclusively by the thermal emission of the canopy (Fig. 2(a)). In contrast, SMOS-based τ_C are also affected by forest ground-emission (Fig. 2(b)) which can cause retrieval crosstalk predominantly from ε_G to τ_C. iii) Different auxiliary temperature data are used in local τ_C (T_{Air} and $T_C = T_{\mathrm{Tree}}$) and SMOS-based τ_C (T_{Air} and $T_C = T_G$ and Ground roughness parameters $\{h_G, q_G, n^V_G, n^H_G\}$.

Fig. 8 shows a number of time-series, each of which include the SMOS study period, 1 February 2019 to 31 May 2019. Red squares and crosses in Fig. 8(a) represent, respectively, average in-situ Air temperature T_{Air} and effective Ground temperature T_G (Section 2.2) measured during AM day-hours 05:00 – 07:00. Blue open squares and crosses in Fig. 8(b) show corresponding temperatures for the PM day-hours 17:00 – 19:00. For comparison with in-situ T_{Air} and T_G, Fig. 8(a) and (b) also include simulated $T_{\mathrm{Air,ECMWF}}$ (green dashed line) and $T_{\mathrm{Surf,ECMWF}}$ (green solid line) from the European Centre for Medium-Range Weather Forecasts (ECMWF). The latter are processed specifically for operational SMOS retrievals over the "Sodankylä grid cell". They are interpolated in time and space to suit the SMOS "Sodankylä grid cell" at local overpassing time at AM ~ 06:00 and PM ~ 18:00. However, SMOS-based (τ_C, ε_G), retrieved and analyzed here, use in-situ temperatures $T_C = T_{\mathrm{Air}}$ and T_G to represent Canopy- and effective Ground temperature. Fig. 8(c) depicts the evolution of Snow Depth (*SD*) measured at the FMI-ARC. The time-series of τ_C and ε_G retrieved from SMOS L3TB are shown in Fig. 8(d) and (e), respectively, for AM-orbits (red solid squares) and PM-orbits (blue open squares).

Effective Ground temperature T_G for AM hours and PM hours show the "zero-degree curtain", as is typical for a partial frozen soil surface below snow, despite T_{Air} rising above 0 °C several times during the study period. Furthermore, Snow-Depth *SD* indicates rapid thawing of the ground surface ($T_G > 0$ °C) after snow-clearance on ~ 14 May 2019 due to the loss of the snowpack's thermal insulation. Apart from a few exceptions (29 March 2019, 9 May 2019, 14 May 2019) retrieved effective Ground permittivity is $\varepsilon_G < 12$. This implies that during the SMOS study period (1 February 2019 – 31 May 2019) microwave emission from the ground compartment (soil, litter, snow) is relatively stable.

Comparisons between in-situ T_G and respective simulated $T_{\mathrm{Surf,ECMWF}}$ show close agreement. However, T_{Air} and respective $T_{\mathrm{Air,ECMWF}}$ deviate from each other considerably. Most prominent, during AM hours 05:00 – 07:00, lowest and highest values of in-situ T_{Air} are over- and under-estimated by simulated $T_{\mathrm{Air,ECMWF}}$, sometimes by more than 10 K as is apparent from Fig. 8(a). Specially in the context of the exploration of L-VOD's temperature dependence, selection of temperature data that is most representative of Canopy temperature T_C is crucial to i) retrieve (τ_C, ε_G), and ii) to analyze the temperature response $\tau_C(T_C)$.

In operational SMOS two-parameter retrievals of L-VOD τ_C and Soil Moisture *SM*, Canopy temperature T_C is represented by $T_{\mathrm{Air,ECMWF}}$. This assumes that temperature gradients within the canopy are minimal during SMOS AM (~ 06:00) and PM (~ 18:00) overpasses around dawn (Kerr et al., 2012). Considering the mentioned differences between in-situ and ECMWF temperatures, we use in-situ temperatures instead of ECMWF simulated temperatures in our SMOS retrievals (τ_C, ε_G) and in the analysis of L-VOD's temperature dependence. It is worth to mention that when representing canopy- and effective ground temperature by $T_{\mathrm{Air,ECMWF}}$ and $T_{\mathrm{Surf,ECMWF}}$ instead of in-situ T_{Air} and T_G, resulting L-VOD's temperature response is less apparent and less consistent with corresponding findings from close-range observations (Section 4.1) and theory (Section 3.3).

The temporal evolution of $T_C = T_{\mathrm{Air}}$ (Fig. 8(a, b)), as well as τ_C retrieved from SMOS L3TB (Fig. 8(d)), show nothing more than increasing trends with progressing time. However, Fig. 9 sheds light on the temperature dependence $\tau_C(T_C)$. L-VOD retrieved from SMOS AM-(Fig. 9(a)) and PM-orbits (Fig. 9(b)) over the "Sodankylä grid cell" are color-coded to indicate dates of measurement during the time-period 1 February 2019 – 31 May 2019 shown in Fig. 8. Black lines show simulated $\tau_C(T_C)$ using the parameters listed in Table 1 and the optimized L-VOD model parameters $\{WC_{\mathrm{Wood}}, S_{\mathrm{Water}}\}$ and $\{T_{\mathrm{melt}}, \varepsilon''_{\mathrm{Wood\text{-}Cells}}\}$ minimizing the RMSD between SMOS-based and simulated L-VOD. As outlined in Section 3.3.2, the parameters $\{WC_{\mathrm{Wood}}, S_{\mathrm{Water}}\}$ predominantly affect τ_C for $T_C > 0$ °C, while main impacts of $\{T_{\mathrm{melt}}, \varepsilon''_{\mathrm{Wood\text{-}Cells}}\}$ are on τ_C for $T_C \lesssim -T_{\mathrm{melt}}$. Values of the optimized two parameter-pairs as well as RMSD and R^2 of the L-VOD model-fit are provided in Fig. 9.

Temperature dependence $\tau_C(T_C)$ of L-VOD retrieved from SMOS (Fig. 9) follows the theoretically expected behavior (Fig. 4). Typically, SMOS-based L-VOD are maximal at $T_C \approx 0$ °C, which is most often the case during the second-half of March (green and cyan data points). With decreasing $T_C \leq 0$ °C, SMOS-based τ_C decrease distinctly and approach

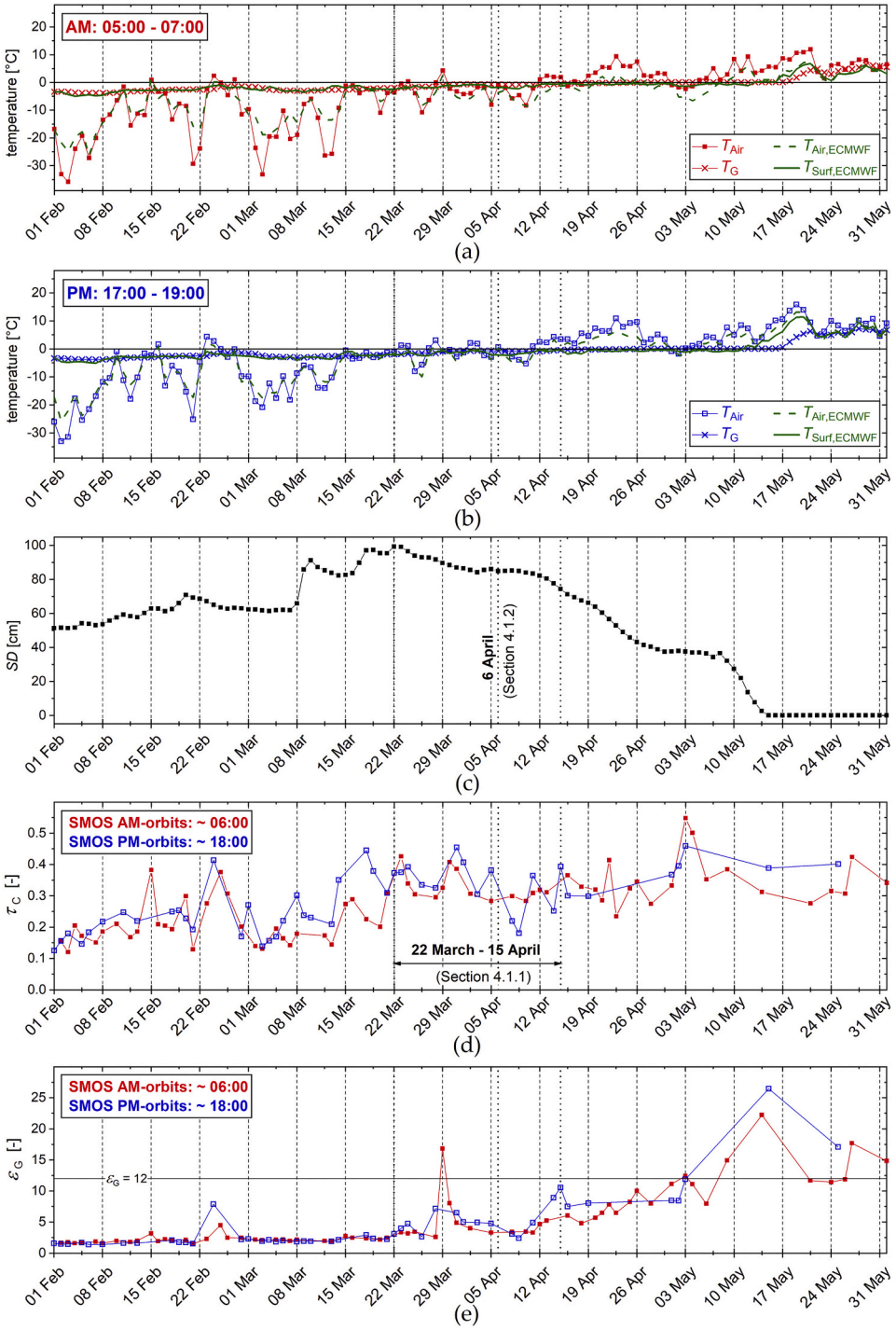

Fig. 8. Time-series of in-situ Air- and effective Ground temperature T_{Air}, T_G, and simulated ECMWF Air- and Surface temperature $T_{Air,ECMWF}$, $T_{Surf,ECMWF}$ during (a) AM day-hours 05:00 – 07:00 and (b) during PM day-hours 17:00 – 19:00. (c) Snow Depth (*SD*) measured at FMI-ARC, (d) L-VOD τ_C, and (e) effective Ground permittivity ε_G retrieved from SMOS L3TB over the "Sodankylä grid cell" measured for AM (~ 06:00) and PM (~ 18:00) orbits.

their minimum at lowest temperatures, present during February (red and orange data points). With increasing $T_C > 0$ °C, mostly occurring after the second-half of April (light and dark blue data points), L-VOD also show a decreasing trend. As mentioned earlier, the peak of L-VOD at $T_C \approx 0$ °C should not be interpreted as a result of changing forest phenology (such as gain in biomass due to growth or rehydration), but rather due to the EM considerations included in the developed L-VOD model (Section 3.3).

Absolute values of τ_C retrieved from SMOS L3TB over the "Sodankylä grid cell" (Fig. 9) are ~ 1.5 times larger than τ_C derived from close-range $T^p_{B,B\text{-}C}$ (Fig. 6) measured at the forest stand at FMI-ARC. This is somewhat expected considering the mentioned different spatial scales as well as the fundamentally different observation and retrieval methods. This quantitative difference is reflected in different values of the L-VOD model parameters optimized to match L-VOD at the local- and at the SMOS scale, indicated in Figs. 6 and 9, respectively. However, in both cases, values of $\{WC_{Wood}, S_{Water}\}$ and $\{T_{melt}, \varepsilon''_{Wood\text{-}Cells}\}$ fall within meaningful ranges, demonstrating that the L-VOD model is capable of explaining the temperature dependence $\tau_C(T_C)$ at the local scale as well as at the scale of the SMOS "Sodankylä grid cell".

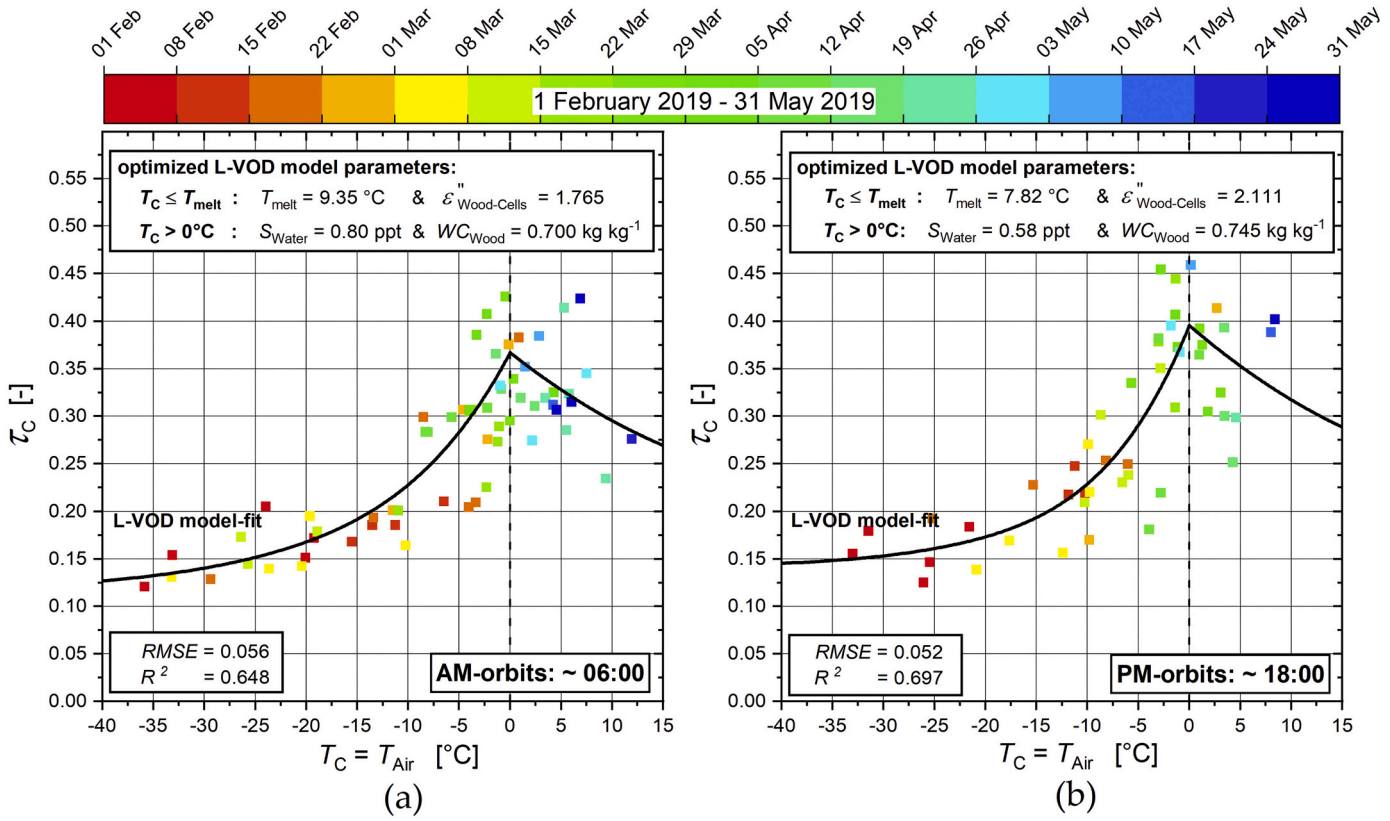

Fig. 9. Scatter-plots of Canopy temperature $T_C = T_{Air}$ versus L-VOD τ_C retrieved from SMOS L3TB measured for (a) AM- (~ 06:00) and (b) PM-orbits (~ 18:00) over the "Sodankylä grid cell" during the period 1 February 2019 – 31 May 2019. Date of measurements are color-coded. Lines are $\tau_C(T_C)$ simulated with the L-VOD model (Section 3.3). Values of optimized model parameters are indicated. Further model parameter considered as constants are listed in Table 1. (For interpretation of the references to color in this figure legend, the reader is referred to the web version of this article.)

L-VOD retrieved from ascending AM-orbits and descending PM-orbits, show an increasing trend with time, and are often time correlated to each other as is seen in Fig. 8(d). However, with only a few exceptions, τ_C retrieved from AM-orbits (red in Fig. 8(d)) are smaller than τ_C retrieved from PM-orbits (blue in Fig. 8(d)). This systematic difference leads to the ~ 4 % smaller L-VOD retrieved from AM-orbits (Fig. 9(a)) compared to corresponding ones retrieved from PM-orbits (Fig. 9(b)). This offset is mostly explained by SMOS observational reasons, and not associated with a systematic diurnal cycle in three phenology, which is especially unlikely for a frozen canopy.

As apparent from Fig. 9, $\tau_C(T_C)$ from AM- and PM-orbits are consistent with theory, and similar to each other. Therefore, respective L-VOD model parameters $\{T_{melt}, \varepsilon''_{Wood\text{-}Cells}\} = \{9.35\ °C, 1.765\}$ and $\{T_{melt}, \varepsilon''_{Wood\text{-}Cells}\} = \{7.82\ °C, 2.111\}$ are similar to each other, but they exceed $\{T_{melt}, \varepsilon''_{Wood\text{-}Cells}\} = \{2.06\ °C, 0.945\}$ optimized to match L-VOD derived from close-range $T^p_{B,B\text{-}C}$ (Fig. 6). Keep in mind, T_{melt} expresses the melt rate of wood sap-water, while $\varepsilon''_{Wood\text{-}Cells}$ determines the minimum of τ_C, approached for deeply frozen conditions ($T_C \ll -T_{melt}$). Thus, the relation between $\varepsilon''_{Wood\text{-}Cells}$, associated with L-VOD from close-range and SMOS brightness temperatures, is consistent with the lower L-VOD seen at the local-scale than at the SMOS-scale. For local L-VOD, $T_{melt} = 2.06$ °C is approximately four-times smaller than $T_{melt} = \{9.35\ °C, 7.82\ °C\}$ estimated from SMOS-based τ_C. This is because T_{melt} estimated from SMOS-based τ_C over the "Sodankylä grid cell" is an effective parameter. It represents a spatial average of the melt rate of wood sap-water referenced to $T_C = T_{Air}$. Another reason is the different representation $T_C = T_{Tree}$ and $T_C = T_{Air}$ of Canopy temperature at the local- and the SMOS-scale.

The parameters $\{WC_{Wood}, S_{Water}\} = \{0.700\ \text{kg kg}^{-1}, 0.80\ \text{ppt}\}$ and $\{WC_{Wood}, S_{Water}\} = \{0.745\ \text{kg kg}^{-1}, 0.58\ \text{ppt}\}$ (Fig. 9) optimized to match SMOS AM and PM L-VOD for unfrozen canopy deviate from each other and from $\{WC_{Wood}, S_{Water}\} = \{0.516\ \text{kg kg}^{-1}, 0.23\ \text{ppt}\}$ (Fig. 6) optimized to match local L-VOD. It is recalled that WC_{Wood} has a "positive scaling effect" on τ_C, while S_{Water} scales both the decreasing gradient of τ_C (Table 2) and also the level of τ_C with increasing $T_C > 0$ °C (Fig. 4). Accordingly, the lower L-VOD at the local-scale than at the SMOS-scale is consistent with the respective different values of optimized parameters WC_{Wood} and S_{Water}. The value $S_{Water} = 0.58$ ppt computed from SMOS PM-orbits (Fig. 9(b)) may lack significance because of the relatively low maximal $T_C \approx 8.4$ °C available during successful τ_C-retrievals for SMOS PM-orbits, compared to the maximum $T_C \approx 12$ °C available during SMOS AM-orbits.

In addition to the polarization-averaged $\tau_C \equiv (\tau^H_C + \tau^V_C)/2$ shown in Fig. 8(d) and Fig. 9, we also tried to retrieve $(\tau^H_C, \varepsilon^H_G)$ and $(\tau^V_C, \varepsilon^V_G)$ separately from SMOS multi-angle $T^{H,\theta}_{B,SMOS,T\text{-}A}$ and $T^{V,\theta}_{B,SMOS,T\text{-}A}$ over the "Sodankylä grid cell". This trial was not successful; accordingly, the finding $\tau^H_C > \tau^V_C$ (Fig. 7(a)), achieved from close-range $T^H_{B,B\text{-}C}$ and $T^V_{B,B\text{-}C}$, could not be corroborated by means of SMOS-based retrievals τ^H_C and τ^V_C. However, the finding that predominant horizontal orientation of branches causes $\tau^H_C > \tau^V_C$ is not called into question. Rather, it indicates that simultaneous retrieval of canopy- and ground properties from multi-angle SMOS brightness temperatures inevitably requires both polarizations.

5. Summary and conclusions

Exploration of ElectroMagnetic (EM) reasons for the dependency $\tau_C(T_C)$ of L-VOD on Canopy temperature T_C is the central theme of this study. It is shown that τ_C of a typical boreal forest is impacted by T_C via its impact on the dielectric properties of sap-water. It is found that L-VOD is typically maximal at around 0 °C and decreases toward negative and positive temperatures. The developed L-VOD model explains this

temperature-dependency by freezing wood sap-water at $T_C \lesssim 0$ °C and by the temperature response of the permittivity of liquid sap-water for $T_C > 0$ °C. This characteristic temperature response $\tau_C(T_C)$ was demonstrated at different spatial- and temporal scales, namely for the boreal forest stand at FMI-ARC and for the SMOS "Sodankylä grid cell" dominated by boreal forest (areal fraction >93 %) of the similar type.

The gained insight into the drop of L-VOD due to freezing finds valuable practical applications. For instance, it explains the larger seasonal dynamics in L-VOD observed for boreal forests than for temperate forests (Mialon et al., 2020). A sharp decrease in both co- and cross polarized backscatter for temperatures $T_C < 0$ °C has also been recognized at P- and L-band backscatter (Monteith, 2020). The demonstrated milder decrease of L-VOD with increasing temperature above the melting point is currently primarily of academic value. Future studies on temperate or tropical forests may reveal the theoretically expected decrease of L-VOD with increasing temperature. Ultimately, L-VOD retrieved at a given T_C could be compensated for the now understood EM reasons causing $\tau_C(T_C)$ to provide temperature normalized L-VOD. Its potentially improved explanatory power in terms of forest phenology, AGB or LAI is subject to future investigations. For now, the demonstrated and explained temperature sensitivity $\tau_C(T_C)$ indicates that users should interpret L-VOD of boreal forests during transitions between frozen and thawed times with caution. This is because in addition to vegetation growth or rehydration, L-VOD also changes due to EM reasons related to the high permittivity of liquid-water compared to ice and the temperature dependence of sap-water permittivity.

During the late-winter to spring periods, consistent L-VOD temperature dependencies $\tau_C(T_C)$ are observed at the substantially different local- and SMOS scales. Absolute values of L-VOD retrieved from SMOS L3TB are larger than local L-VOD computed from downwelling $T^{p}_{B,B\text{-}C}$ measured from Below the tree Canopy. At the local-scale, temperature dependence $\tau_C(T_C)$ during the 4-week period from 22 March 2019 to 15 April 2019 is consistent with that observed for 6 April 2019. The respective inter-diurnal variability of L-VOD is significant. This variability is the result of below- and above ~ 0 °C temperatures leading to partially frozen and thawed canopy. It indicates that L-VOD retrieved from satellite observations can depend noticeably on the local time of overpass, especially during transitional periods, when forests undergo diurnal freeze-thaw.

Additionally, it is found that L-VOD τ_C^H derived from close-range $T_{B,B\text{-}C}{}^H$ at horizontal polarization is larger than τ_C^V derived from $T^V_{B,B\text{-}C}$ at vertical polarization. $\tau_C^H > \tau_C^V$ is explained by predominantly horizontal orientation of branches, and it is consistent with previous findings made in deciduous forests. However, demonstration of $\tau_C^H > \tau_C^V$ for the SMOS "Sodankylä grid cell" failed because simultaneous retrieval of canopy- and ground properties from multi-angle SMOS brightness temperatures inevitably requires both polarizations.

Demonstration of the characteristic temperature response $\tau_C(T_C)$ by means of SMOS brightness temperatures is a delicate task necessitating practical considerations. In particular, the choice of data used to represent canopy- and ground temperature is critical to uncover the proven but moderate decrease of L-VOD τ_C of unfrozen canopy with increasing Canopy temperature $T_C \gtrsim 0$ °C. This branch of the L-VOD's temperature sensitivity $\tau_C(T_C)$ is nearly invisible when ECMWF simulated air temperatures are used for T_C (as is the case in operational SMOS Level-2 and SMOS-IC retrievals). Thus, we used in-situ temperatures instead of ECMWF simulated temperatures to demonstrate $\tau_C(T_C)$ derived from close-range and SMOS brightness temperatures. In turn, the degree of visibility of EM-induced $\tau_C(T_C)$ observable in satellite-based L-VOD could be utilized as an indicator to assess representativeness of auxiliary data (canopy temperatures, for instance) used in the retrieval. Another future practical application of the gained knowledge concerns estimation of forest state-parameters such as AGB and canopy Integrated Liquid Water (ILW) from retrieved L-VOD τ_C and inversion of the developed L-VOD model.

Acknowledgements

The work is supported by the European Space Agency (ESA) Living Planet Fellowship "LOSTinFTC" (Contract No. 4000130910/20/I-NS) and the ESA project "SMOS Expert Support Laboratory for Level 2 Soil Moisture" (Contract no. 4000125649). The ELBARA-II radiometers used in this study are on loan from ESA (Contract No. 21013/07/NL/FF)". Further, the authors would like to thank Dr. Urs Wegmüller (Remote Sensing Research and Consulting AG) for editing the manuscript and for his helpful scientific comments.

Appendix

Maxwell garnett mixing rule for randomly oriented, highly prolate, rotation-symmetric ellipsoidal inclusions

Eq. (12) used to compute the Canopy layers' effective permittivity ε_C required in Eq. (11) to compute the power absorption coefficient α_C within the Canopy layer is established subsequently: In section 9.3.2 of the book "Electromagnetic mixing formulas and applications" (Sihvola, 1999) the Maxwell Garnett mixing rule used to compute the effective permittivity of a two-phase medium consisting of randomly oriented ellipsoids of any axial ratio included in a dielectric background is provided. It assumes that dielectric inclusions are, at least along one direction, much smaller than the wavelength λ of the propagating wave. Under consideration of the notation used here, the respective eq. (9.9) in Sihvola, 1999 reads:

$$\varepsilon_C = \varepsilon_{Air} + \varepsilon_{Air}\frac{\nu_{SCC}/3\cdot\sum\limits_{j=\{x,y,z\}}\frac{\varepsilon_{Wood}-\varepsilon_{Air}}{\varepsilon_{Air}+N_j\cdot(\varepsilon_{Wood}-\varepsilon_{Air})}}{1-\nu_{SCC}/3\cdot\sum\limits_{j=\{x,y,z\}}\frac{N_j\cdot(\varepsilon_{Wood}-\varepsilon_{Air})}{\varepsilon_{Air}+N_j\cdot(\varepsilon_{Wood}-\varepsilon_{Air})}} \quad (23)$$

The Small Canopy Constituents (SCC) of Volume fraction ν_{SCC} and permittivity ε_{Wood} embedded in the air background of permittivity $\varepsilon_{Air} = 1$ represent branches, which are most determinative for L-VOD τ_C of a forest Canopy (Ferrazzoli and Guerriero, 1996). In the L-VOD model branches (SCC) are mimicked as highly prolate rotation-symmetric ellipsoids with half-axis a_j along their orthogonal directions $j = \{x, y, z\}$ fulfilling $a_x > a_y = a_z$. Respective depolarization factors N_j are given by eqs. (4.7) and (4.8) in section 4.2.1 in Sihvola, 1999:

$$N_x = \left(1-e^2\right)/\left(2\cdot e^3\right)\cdot\left[\ln\left((1+e)/(1-e)\right)-2\cdot e\right] \text{ and } N_y = N_z = 1/2\cdot(1-N_x) \quad (24)$$

Eccentricity e of an ellipsoid is defined via its Aspect Ratio AR between the short half-axis $a_y = a_z$ and the long half-axis a_x:

$$e \equiv \sqrt{1-AR^2} \text{ with } AR = a_z/a_x \quad (25)$$

Naturally, eccentricity and Aspect Ratio of a sphere of radius $r = a_z = a_y = a_x$ is $e = 0$ and $AR = 1$, while eccentricity and Aspect Ratio of a highly prolate axial-symmetric ellipsoid is $e \lesssim 1$ and $AR \gtrsim 0$. In other words, thin and long branches (SCC) exhibit small AR.

Using Eqs. (24) and (25) in the Maxwell Garnett mixing rule (23) yields effective permittivity ε_C of the canopy layer expressed by AR. Because AR is a small number in case of highly prolate axial-symmetric ellipsoidal SCC, the resulting expression for ε_C can be approximated by a Taylor series in AR at $AR = 0$. The resulting second order power-series leads to Eq. (12) used in the L-VOD model. It reads:

$$\varepsilon_C = \varepsilon_{Air} + \frac{(\varepsilon_{Wood} - \varepsilon_{Air})\cdot(\varepsilon_{Wood} + 5\cdot\varepsilon_{Air})\cdot\nu_{SCC}}{3\cdot(\varepsilon_{Wood} + \varepsilon_{Air}) - 2\cdot(\varepsilon_{Wood} - \varepsilon_{Air})\cdot\nu_{SCC}} + \mathcal{O}[AR]^2 \quad (26)$$

References

Al Bitar, A., Mialon, A., Kerr, Y.H., Cabot, F., Richaume, P., Jacquette, E., Quesney, A., Mahmoodi, A., Tarot, S., Parrens, M., 2017. The global SMOS level 3 daily soil moisture and brightness temperature maps. Earth Syst. Sci. Data 9, 293–315.

Brandt, M., Wigneron, J.-P., Chave, J., Tagesson, T., Penuelas, J., Ciais, P., Rasmussen, K., Tian, F., Mbow, C., Al-Yaari, A., 2018. Satellite passive microwaves reveal recent climate-induced carbon losses in African drylands. Nat. Ecol. Evol. 2, 827–835.

Carlson, T.N., Ripley, D.A., 1997. On the relation between NDVI, fractional vegetation cover, and leaf area index. Remote Sens. Environ. 62, 241–252.

Carr, R., 2021. Simulated Annealing. From MathWorld – A Wolfram Web Resource, created by Eric W. Weisstein. https://mathworld.wolfram.com/SimulatedAnnealing.html.

Chanzy, A., Kerr, Y., Wigneron, J.-P., Calvet, J.-C., 1997. Soil moisture estimation under sparse vegetation using microwave radiometry at C-band. In: IGARSS'97. 1997 IEEE International Geoscience and Remote Sensing Symposium Proceedings. Remote Sensing-A Scientific Vision for Sustainable Development. IEEE, pp. 1090–1092.

Chaparro, D., Duveiller, G., Piles, M., Cescatti, A., Vall-Llossera, M., Camps, A., Entekhabi, D., 2019. Sensitivity of L-band vegetation optical depth to carbon stocks in tropical forests: a comparison to higher frequencies and optical indices. Remote Sens. Environ. 232, 111303.

Chapin Iii, F., McGuire, A., Randerson, J., Pielke, R., Baldocchi, D., Hobbie, S.E., Roulet, N., Eugster, W., Kasischke, E., Rastetter, E., 2000. Arctic and boreal ecosystems of western North America as components of the climate system. Glob. Chang. Biol. 6, 211–223.

Choudhury, B., Schmugge, T., Mo, T., 1982. A parameterization of effective soil temperature for microwave emission. J. Geophys. Res. 87, 1301–1304.

Ding, W.-D., Koubaa, A., Chaala, A., Belem, T., Krause, C., 2008. Relationship between wood porosity, wood density and methyl methacrylate impregnation rate. Wood Mater. Sci. Eng. 3, 62–70.

Fernandez-Moran, R., Wigneron, J.-P., Lopez-Baeza, E., Salgado-Hernanz, P.M., Mialon, A., Miernecki, M., Alyaari, A., Parrens, M., Schwank, M., Wang, S., Coll-Pajaron, A., Lawrence, H., Kerr, Y.H., 2014. Evaluating the impact of roughness in soil moisture and optical thickness retrievals over the VAS area. In: IGARSS 2014 and the 35th Canadian Symposium on Remote Sensing, CSRS 2014. Quebec Convention Centre Quebec City, Canada, pp. 1947–1950.

Fernandez-Moran, R., Al-Yaari, A., Mialon, A., Mahmoodi, A., Al Bitar, A., De Lannoy, G., Rodriguez-Fernandez, N., Lopez-Baeza, E., Kerr, Y., Wigneron, J.-P., 2017. SMOS-IC: an alternative SMOS soil moisture and vegetation optical depth product. Remote Sens. 9, 457.

Ferrazzoli, P., Guerriero, L., 1996. Passive microwave remote sensing of forests: a model investigation. IEEE Trans. Geosci. Remote Sens. 34, 433–443.

Foster, J.L., Sun, C., Walker, J.P., Kelly, R., Chang, A., Dong, J., Powell, H., 2005. Quantifying the uncertainty in passive microwave snow water equivalent observations. Remote Sens. Environ. 94, 187–203.

Frappart, F., Wigneron, J.-P., Li, X., Liu, X., Al-Yaari, A., Fan, L., Wang, M., Moisy, C., Le Masson, E., Lafkih, Z.A., 2020. Global monitoring of the vegetation dynamics from the Vegetation Optical Depth (VOD): a review. Remote Sens. 12, 2915.

Guglielmetti, M., Schwank, M., Mätzler, C., Oberdörster, C., Vanderborght, J., Flühler, H., 2007. Measured microwave radiative transfer properties of a deciduous forest canopy. Remote Sens. Environ. 523–532.

Guglielmetti, M., Schwank, M., Mätzler, C., Oberdörster, C., Vanderborght, J., Flühler, H., 2008. FOSMEX: forest soil moisture experiments with microwave radiometry. IEEE Trans. Geosci. Remote Sens. 46, 727–735.

Houtz, D., Naderpour, R., Schwank, M., Steffen, K., 2019. Snow wetness and density retrieved from L-band satellite radiometer observations over a site in the West Greenland ablation zone. Remote Sens. Environ. 235, 111361.

Huete, A., Justice, C., Liu, H., 1994. Development of vegetation and soil indices for MODIS-EOS. Remote Sens. Environ. 49, 224–234.

Jackson, T., Schmugge, T., 1991. Vegetation Effects on the Microwave Emission of Soils.

Jia, G.J., Epstein, H.E., Walker, D.A., 2009. Vegetation greening in the Canadian Arctic related to decadal warming. J. Environ. Monit. 11, 2231–2238.

Jonard, F., Weihermüller, L., Jadoon, K.Z., Schwank, M., Vereecken, H., Lambot, S., 2011. Mapping field-scale soil moisture with L-band radiometer and ground-penetrating radar over bare soil. IEEE Trans. Geosci. Remote Sens. 49, 2863–2875.

Kawabata, A., Ichii, K., Yamaguchi, Y., 2001. Global monitoring of interannual changes in vegetation activities using NDVI and its relationships to temperature and precipitation. Int. J. Remote Sens. 22, 1377–1382.

Kerr, Y., Waldteufel, P., Wigneron, J.-P., Martinuzzi, J.-M., Font, J., Berger, M., 2001. Soil moisture retrieval from space: the soil moisture and ocean salinity (SMOS) mission. IEEE Trans. Geosci. Remote Sens. 39, 1729–1735.

Kerr, Y.H., Waldteufel, P., Wigneron, J.P., Delwart, S., Cabot, F., Boutin, J., Escorihuela, M.J., Font, J., Reul, N., Gruhier, C., Juglea, S.E., Drinkwater, M.R., Hahne, A., Martin-Neira, M., Mecklenburg, S., 2010. The SMOS mission: new tool for monitoring key elements of the global water cycle. Proc. IEEE 98, 666–687.

Kerr, Y.H., Waldteufel, P., Richaume, P., Wigneron, J.P., Ferrazzoli, P., Mahmoodi, A., Al Bitar, A., Cabot, F., Gruhier, C., Juglea, S.E., Leroux, D., Mialon, A., Delwart, S., 2012. The SMOS soil moisture retrieval algorithm. IEEE Trans. Geosci. Remote Sens. 50, 1384–1403.

Kerr, Y., Richaume, P., Waldteufel, P., Ferrazzoli, P., Wigneron, J.P., Schwank, M., Rautiainen, K., 2020. SMOS Level 2 Processor soil Moisture Algorithm Theoretical Basis Document (ATBD). SM-ESL (CBSA), CESBIO, Toulouse. SO-TN-ESL-SM-GS-0001-4b, 145.

Kirkpatrick, S., Gelatt, C.D., Vecchi, M.P., 1983. Optimization by simulated annealing. Science 220, 671–680.

Klein, L., Swift, C., 1977. An improved model for the dielectric constant of sea water at microwave frequencies. IEEE J. Ocean. Eng. 2, 104–111.

Lemmetyinen, J., Schwank, M., Derksen, C., Roy, A., Colliander, A., Rautiainen, K., Pulliainen, J., 2016a. Retrieval of snow parameters from L-band observations-application for SMOS and SMAP. In: 2016 IEEE International Geoscience and Remote Sensing Symposium (IGARSS). IEEE, pp. 7067–7070.

Lemmetyinen, J., Schwank, M., Rautiainen, K., Kontu, A., Parkkinen, T., Mätzler, C., Wiesmann, A., Wegmüller, U., Derksen, C., Toose, P., Roy, A., Pulliainen, J., 2016b. Snow density and ground permittivity retrieved from L-band radiometry: application to experimental data. Remote Sens. Environ. 180, 377–391.

Li, Q., Kelly, R., Leppänen, L., Vehviläinen, J., Kontu, A., Lemmetyinen, J., Pulliainen, J., 2019. The influence of thermal properties and canopy-intercepted snow on passive microwave transmissivity of a scots pine. IEEE Trans. Geosci. Remote Sens. 57, 5424–5433.

Li, X., Al-Yaari, A., Schwank, M., Fan, L., Frappart, F., Swenson, J., Wigneron, J.-P., 2020. Compared performances of SMOS-IC soil moisture and vegetation optical depth retrievals based on Tau-Omega and Two-Stream microwave emission models. Remote Sens. Environ. 236, 111502.

Magnani, F., Mencuccini, M., Borghetti, M., Berbigier, P., Berninger, F., Delzon, S., Grelle, A., Hari, P., Jarvis, P.G., Kolari, P., 2007. The human footprint in the carbon cycle of temperate and boreal forests. Nature 447, 849–851.

Mätzler, C., 1987. Applications of the interaction of microwaves with the seasonal snow cover. Remote Sens. Rev. 2, 259–387.

Mätzler, C., 1994. Microwave transmissivity of a forest canopy: experiments made with a beech. Remote Sens. Environ. 48, 172–180.

Mätzler, C., 1996. Notes on Microwave Radiation from Snow Samples and Emission of Layered Snowpacks. Institute of Applied Physics (IAP) at the University of Bern, Switzerland updated 2004.

Mätzler, C., 2006. Thermal Microwave Radiation: Applications for Remote Sensing. IEE Electromagnetic Waves Series No. 52, London, UK.

Mätzler, C., Wiesmann, A., 2012. Documentation for MEMLS, Version 3 'Microwave Emission Model of Layered Snowpacks'. Institute of Applied Physics (IAP) at the University of Bern, Switzerland.

Mätzler, C., Weber, D., Wüthrich, M., Schneeberger, K., Stamm, C., Wydler, H., Flühler, H., 2003. ELBARA, the ETH L-band radiometer for soil-moisture research. In: Proceedings of International Geoscience and Remote Sensing Symposium (IGARSS). IEEE, Toulouse, France, pp. 3058–3060.

Mialon, A., Rodríguez-Fernández, N.J., Santoro, M., Saatchi, S., Mermoz, S., Bousquet, E., Kerr, Y.H., 2020. Evaluation of the sensitivity of SMOS L-VOD to forest above-ground biomass at global scale. Remote Sens. 12, 1450.

Miernecki, M., Wigneron, J.-P., Lopez-Baeza, E., Kerr, Y., Jeu, R.D., Lannoy, G.J.M.D., Jackson, T.J., O'Neill, P.E., Schwank, M., Moran, R.F., Bircher, S., Lawrence, H., Mialon, A., Bitar, A.A., Richaume, P., 2014. Comparison of SMOS and SMAP soil moisture retrieval approaches using tower-based radiometer data over a vineyard field. Remote Sens. Environ. 154, 89–101.

Monteith, A., 2020. Temporal Characteristics of Boreal Forest Radar Measurements. Chalmers Tekniska Hogskola, Sweden.

Naderpour, R., Schwank, M., 2018. Snow wetness retrieved from L-band radiometry. Remote Sens. 10, 359.

Naderpour, R., Schwank, M., Mätzler, C., 2017a. Davos-Laret remote sensing field laboratory: 2016/2017 winter season L-band measurements data-processing and analysis. Remote Sens. 9, 1185.

Naderpour, R., Schwank, M., Mätzler, C., Lemmetyinen, J., Steffen, K., 2017b. Snow density and ground permittivity retrieved from L-band radiometry: a retrieval sensitivity analysis. IEEE J. Select. Top. Appl. Earth Observ. Remote Sens. 10, 3148–3161.

Naderpour, R., Houtz, D., Schwank, M., 2020. Snow wetness retrieved from close-range L-band radiometry in the western Greenland ablation zone. J. Glaciol. 1–12.

Olmi, R., Bini, M., Ignesti, A., Riminesi, C., 2000. Dielectric properties of wood from 2 to 3 GHz. J. Microw. Power Electromagn. Energy. 35, 135–143.

Pellarin, T., Wigneron, J.-P., Calvet, J.C., Berger, M., Douville, H., Ferrazzoli, P., Kerr, Y. H., Lopez-Baesa, E., Pulliainen, J., Simmonds, L.P., Waldteufel, P., 2003. Two-year global simulation of L-band brightness temperatures over land. IEEE Trans. Geosci. Remote Sens. 41, 2135–2139.
Pellarin, T., Mialon, A., Biron, R., Coulaud, C., Gibon, F., Kerr, Y., Lafaysse, M., Mercier, B., Morin, S., Redor, I., Schwank, M., Völksch, I., 2016. Three years of L-band brightness temperature measurements in a mountainous area: topography, vegetation and snowmelt issues. Remote Sens. Environ. 2016, 85–98.
Pickett, H.M., Hardy, J.C., Farhoomand, J., 1984. Characterization of a dual-mode horn for submillimeter wavelengths. IEEE Trans. Microw. Theory Tech. 32, 936–937.
Pulliainen, J., Aurela, M., Laurila, T., Aalto, T., Takala, M., Salminen, M., Kulmala, M., Barr, A., Heimann, M., Lindroth, A., 2017. Early snowmelt significantly enhances boreal springtime carbon uptake. Proc. Natl. Acad. Sci. 114, 11081–11086.
Rahmoune, R., Ferrazzoli, P., Kerr, Y.H., Richaume, P., 2013. SMOS level 2 retrieval algorithm over forests: description and generation of global maps. IEEE J. Select. Top. Appl. Earth Observ. Remote Sens. 6, 1430–1439.
Rautiainen, K., Lemmetyinen, J., Schwank, M., Kontu, A., Ménard, C.B., Mätzler, C., Drusch, M., Wiesmann, A., Ikonen, J., Pulliainen, J., 2014. Detection of soil freezing from L-band passive microwave observations. Remote Sens. Environ. 147, 206–218.
Richardson, A.D., Keenan, T.F., Migliavacca, M., Ryu, Y., Sonnentag, O., Toomey, M., 2013. Climate change, phenology, and phenological control of vegetation feedbacks to the climate system. Agric. For. Meteorol. 169, 156–173.
Rodríguez-Fernández, N.J., Mialon, A., Mermoz, S., Bouvet, A., Richaume, P., Al Bitar, A., Al-Yaari, A., Brandt, M., Kaminski, T., Le Toan, T., 2018. An evaluation of SMOS L-band vegetation optical depth (L-VOD) data sets: high sensitivity of L-VOD to above-ground biomass in Africa. Biogeosciences 15, 4627–4645.
Roy, A., Toose, P., Mavrovic, A., Pappas, C., Royer, A., Derksen, C., Berg, A., Rowlandson, T., El-Amine, M., Barr, A., 2020. L-band response to freeze/thaw in a boreal forest stand from ground-and tower-based radiometer observations. Remote Sens. Environ. 237, 111542.
Saatchi, S.S., Harris, N.L., Brown, S., Lefsky, M., Mitchard, E.T., Salas, W., Zutta, B.R., Buermann, W., Lewis, S.L., Hagen, S., 2011. Benchmark map of forest carbon stocks in tropical regions across three continents. Proc. Natl. Acad. Sci. 108, 9899–9904.
Schneeberger, K., Schwank, M., Stamm, C., Rosnay, P.d., Mätzler, C., Flühler, H., 2004. Topsoil structure influencing soil water retrieval by microwave radiometry. Vadose Zone J. 3, 1169–1179.
Schwank, M., Mätzler, C., 2006. Air-to-soil transition model. In: Mätzler, C., Rosenkranz, P.W., Battaglia, A., Wigneron, J.P. (Eds.), Thermal Microwave Radiation – Applications for Remote Sensing: IET Electromagnetic Waves Series 52, London, UK.
Schwank, M., Naderpour, R., 2018. Snow density and ground permittivity retrieved from L-band radiometry: melting effects. Remote Sens. 10, 354.
Schwank, M., Stähli, M., Wydler, H., Leuenberger, J., Mätzler, C., Flühler, H., 2004. Microwave L-band emission of freezing soil. IEEE Trans. Geosci. Remote Sens. 42, 1252–1261.
Schwank, M., Mätzler, C., Guglielmetti, M., Flühler, H., 2005. L-band radiometer measurements of soil water under growing clover grass. IEEE Trans. Geosci. Remote Sens. 43, 2225–2237.
Schwank, M., Guglielmetti, M., Mätzler, C., Flühler, H., 2008. Testing a new model for the L-band radiation of moist leaf litter. IEEE Trans. Geosci. Remote Sens. 46, 1982–1994.
Schwank, M., Wiesmann, A., Werner, C., Mätzler, C., Weber, D., Murk, A., Völksch, I., Wegmüller, U., 2010. ELBARA II, an L-band radiometer system for soil moisture research. Sensors MDPI 10, 584–612.
Schwank, M., Wigneron, J.P., Lopez-Baeza, E., Völksch, I., Mätzler, C., Kerr, Y., 2012. L-band radiative properties of vine vegetation at the SMOS Cal/Val site MELBEX III. IEEE Trans. Geosci. Remote Sens. 50, 1587–1601.
Schwank, M., Rautiainen, K., Mätzler, C., Stähli, M., Lemmetyinen, J., Pulliainen, J., Vehviläinen, J., Kontu, A., Ikonen, J., Ménard, C.B., Drusch, M., Wiesmann, A., Wegmüller, U., 2014. Model for microwave emission of a snow-covered ground with focus on L band. Remote Sens. Environ. 154, 180–191.
Schwank, M., Naderpour, R., Mätzler, C., 2018. "Tau-omega"- and two-stream emission models used for passive L-band retrievals: application to close-range measurements over a forest. Remote Sens. 10, 1868.
Scipal, K., Arcioni, M., Chave, J., Dall, J., Fois, F., LeToan, T., Lin, C., Papathanassiou, K., Quegan, S., Rocca, F., Saatchi, S., Shugart, H., Ulander, L., Williams, M., 2010. The BIOMASS mission — an ESA Earth explorer candidate to measure the BIOMASS of the earth's forests. In: 2010 IEEE International Geoscience and Remote Sensing Symposium, pp. 52–55.
Sihvola, A.H., 1999. Electromagnetic Mixing Formulas and Applications. Iet.
Su, Z., Wen, J., Zeng, Y., Zhao, H., Lv, S., van der Velde, R., Zheng, D., Wang, X., Wang, Z., Schwank, M., Kerr, Y., Yueh, S., Colliander, A., Qian, H., Drusch, M., Mecklenburg, S., 2020. Multiyear in-situ L-band microwave radiometry of land surface processes on the Tibetan Plateau. Scientific Data 7, 317.
Torgovnikov, G.I., 1993. Dielectric Properties of Wood and Wood-Based Materials. Springer-Verlag.
Tucker, C.J., 1979. Red and photographic infrared linear combinations for monitoring vegetation. Remote Sens. Environ. 8, 127–150.
Ulaby, F.T., El-Rayes, M.A., 1987. Microwave dielectric spectrum of vegetation-Part II: dual-dispersion model. IEEE Trans. Geosci. Remote Sens. 550–557.
Vittucci, C., Ferrazzoli, P., Kerr, Y., Richaume, P., Guerriero, L., Rahmoune, R., Laurin, G. V., 2016. SMOS retrieval over forests: exploitation of optical depth and tests of soil moisture estimates. Remote Sens. Environ. 180, 115–127.
Vittucci, C., Ferrazzoli, P., Kerr, Y.H., Richaume, P., Laurin, G.V., Guerriero, L., 2018. Analysis of vegetation optical depth and soil moisture retrieved by SMOS over tropical forests. IEEE Geosci. Remote Sens. Lett. 16, 504–508.
Völksch, I., Schwank, M., Mätzler, C., 2010. L-band reflectivity of a wire grid above a dielectric surface. IEEE Trans. Geosci. Remote Sens. Lett. 7, 601–605.
Völksch, I., Schwank, M., Mätzler, C., 2011. L-band reflectivity of a furrowed soil surface. IEEE Trans. Geosci. Remote Sens. 49, 1957–1966.
Völksch, I., Schwank, M., Stähli, M., Mätzler, C., 2015. Relief effects on the L-band emission of a bare soil. Remote Sens. 7, 14327.
Wang, J., Rich, P., Price, K., Kettle, W., 2004. Relations between NDVI and tree productivity in the central Great Plains. Int. J. Remote Sens. 25, 3127–3138.
Wang, Q., Adiku, S., Tenhunen, J., Granier, A., 2005. On the relationship of NDVI with leaf area index in a deciduous forest site. Remote Sens. Environ. 94, 244–255.
Wiesmann, A., Mätzler, C., 1999. Microwave emission model of layered snowpacks. Remote Sens. Environ. 70, 307–316.
Wigneron, J.-P., Laguerre, L., Kerr, Y., 2001. A simple parameterization of the L-band microwave emission from rough agricultural soils. IEEE Trans. Geosci. Remote Sens. 39, 1697–1707.
Wigneron, J.-P., Kerr, Y., Waldteufel, P., Saleh, K., Richaume, P., Ferrazzoli, P., Escorihuela, M.-J., Grant, J.P., Hornbuckle, B., de Rosnay, P., Calvet, J.-C., Pellarin, T., Gurney, R., Mätzler, C., 2007. L-band microwave emission of the biosphere (L-MEB) model: description and calibration against experimental data sets over crop fields. Remote Sens. Environ. 107, 639–655.
Zhang, X., Friedl, M.A., Schaaf, C.B., Strahler, A.H., Hodges, J.C., Gao, F., Reed, B.C., Huete, A., 2003. Monitoring vegetation phenology using MODIS. Remote Sens. Environ. 84, 471–475.
Zheng, D., Wang, X., van der Velde, R., Zeng, Y., Wen, J., Wang, Z., Schwank, M., Ferrazzoli, P., Su, Z., 2017. L-band microwave emission of soil freeze–thaw process in the third pole environment. IEEE Trans. Geosci. Remote Sens. 55, 5324–5338.
Zheng, D., Li, X., Wang, X., Wang, Z., Wen, J., van der Velde, R., Schwank, M., Su, Z., 2019a. Sampling depth of L-band radiometer measurements of soil moisture and freeze-thaw dynamics on the Tibetan Plateau. Remote Sens. Environ. 226, 16–25.
Zheng, D., Wang, X., van der Velde, R., Schwank, M., Ferrazzoli, P., Wen, J., Wang, Z., Colliander, A., Bindlish, R., Su, Z., 2019b. Assessment of soil moisture SMAP retrievals and ELBARA-III measurements in a Tibetan meadow ecosystem. IEEE Geosci. Remote Sens. Lett. 16 (16), 1407–1411.
Zhou, L., Tucker, C.J., Kaufmann, R.K., Slayback, D., Shabanov, N.V., Myneni, R.B., 2001. Variations in northern vegetation activity inferred from satellite data of vegetation index during 1981 to 1999. J. Geophys. Res.-Atmos. 106, 20069–20083.